Ultra-luminous X-ray sources in the most metal poor galaxies

Maria Tsantaki

University of Crete

Supervisor: Andreas Zezas

Heraklio, 2011

Contents

List of Figures

List of Tables

Abstract

We investigated the Ultra-luminous X-ray source (ULX) population in a sample of 25 extremely metal poor galaxies (XMPGs) in the local universe. We processed recent observations from the Chandra X-ray Observatory with the CIAO software and detected 6 X-ray sources in the 0.3-8.0 keV band. We obtained spectra for these sources and found their X-ray luminosities to be in the range $(0.7\text{-}7.5)\times10^{39}$ erg/sec, characterizing them as ULX sources.

In addition, we processed infrared data for these galaxies from the Spitzer Space telescope in the 24 micron band and performed aperture photometry in order to measure their luminosities. We used the 24μm luminosity to estimate their Star Formation Rate (SFR).

Moreover, we compared the XMPGs with 33 galaxies from the Spitzer Infrared Nearby Galaxies Survey (SINGS) sample. For the SINGS galaxies we calculated the SFR using IR and Hα data as well as the number of their ULXs, from the literature. Comparing these samples of different metallicities (High, Intermediate and Low), we reached the conclusion that there is a trend showing that the number of ULXs per SFR is decreasing with metallicity which means that ULXs may prefer metal poor environments. This conclusion comes in agreement with models that derive the ULX population from High Mass X-ray Binaries (HMXBs) with mass transfer through Roche Lobe Overflow (RLO).

1 Introduction

X-Rays are a type of high-energy electromagnetic radiation. X-radiation has a wavelength in the range of 0.01 to 10 nanometers, corresponding to frequencies in the range from 3×10^{16} Hz to 3×10^{19} Hz and energies in the range of 120 eV to 120 keV. X-rays from about 0.12 to 12 keV (10 to 0.10 nm wavelength) are classified as 'soft' X-rays, and from about 12 to 120 keV (0.10 to 0.01 nm wavelength) as 'hard' X-rays, due to their penetrating abilities.

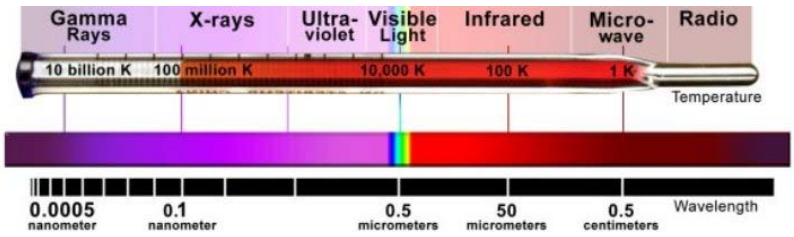

Figure 1: The relation of the frequency of light to the temperature of an object.

X-radiation is absorbed by the atoms and molecules of the Earth's atmosphere, so instruments to detect X-rays must be taken at high altitude by balloons, sounding rockets, or satellites. The discovery of the first cosmic X-ray source was in 1962 when the first X-ray source found in the constellation Scorpius, called Scorpius X-1. As founder in this new field, Riccardo Giacconi received the Nobel Prize in Physics in 2002. X-ray emission is expected in sources which contain extremely hot gas at temperatures from a million to hundred million Kelvin where electrons have very high energies. As of 2007, there were about 550,000 known X-ray sources.

1.1 X-Ray sources

Several types of astrophysical objects emit X-rays, from galaxy clusters and black holes in Active Galactic Nuclei (AGN) to galactic objects such as supernova remnants, stars, and binary stars. These sources can be divided into two general categories: point-like and extended sources.

1.1.1 Point-like sources

Normal stars. Many solar-type stars emit soft X-rays due to coronal activity. This model can explain the X-ray emission from low-mass stars (F, G, K, M spectral type). The coronal X-ray emission from late-type stars is caused by nonradiative heating of a stellar atmosphere. The current view is that these processes are due to the presence of magnetic fields which are generated by a magnetic dynamo. The dynamo generates magnetic fields, which confine and heat the corona. Nearly all coronal heating is directly tied to the magnetic field, which means that if the these stars had no magnetic field, they would have little or no X-ray corona.

Active galactic nuclei. X-rays from AGNs are produced when in-falling matter is heated to temperatures of millions of degrees as it swirls toward the supermassive black hole in the central region of a galaxy, forming an accretion disk. The heating is caused by the disk viscosity as matter moves towards the center. In some AGNs this high-energy matter from the central region is ejected along the rotational axis of the disk in jets with relativistic speeds.

Binaries. There are two distinct groups of X-ray binaries, the Low Mass X-ray Binary (LMXBs) and the High Mass X-ray Binary (HMXBs) depending on the mass of the donor star. Other more peculiar subcategories are Ultraluminous X-ray sources (ULXs), Super-Soft Sources (SSSs) and Quasi-Soft Sources (QSSs).

1.1.2 Extended sources

The Sun. The beginning of the search for X-ray sources above the Earth's atmosphere was on August 5, 1948 by a US Army V-2 rocket. The X-rays that are detected from the Sun actually come from the solar corona, not the solar surface. The corona of the Sun is very hot and tenuous gas blowing away. The temperature of the solar corona is typically above 10^6 K. The dominant emission mechanisms are bremsstrahlung (the emission of radiation when an electron passes by an ion) and atomic line radiation. The luminosity of the Sun in the X-rays ranges from 10^{26} to 10^{27} erg/sec and is therefore a very small fraction of the total energy ($\sim 3.8 \times 10^{33}$ erg/sec) that is generated. The solar X-ray radiation undergoes variations during the course of a solar cycle.

Supernovae remnants. Most of the energy of the supernova explosion is carried off as kinetic energy. This supersonic outflow of stellar ejecta, which itself cools quickly after the explosion, sweeps up and shock heats the surrounding interstellar or circumstellar matter to X-ray temperatures

(this is the primary shock). The swept-up material progressively retards the motion of the ejecta, causing another shock to work its way backwards (in the reference frame of the expanding ejecta), so it too is heated to X-ray temperatures. The result is an extended, diffuse region of X-ray emitting plasma, most of which has temperatures above several million Kelvins.

Normal galaxies. Normal star contribute only a small fraction of the total X-ray luminosity of a galaxy. Most of the X-ray emission of spiral and irregular galaxies comes from a collection of a relatively small number of individual bright sources, such as close accreting binaries with a compact companion, and supernova remnants. In addition, in spiral galaxies diffuse thermal emission has been observed in X-rays from a hot phase of the interstellar medium.

In elliptical galaxies the X-ray emission is due to a hot gaseous component. These galaxies can be ~ 100 times brighter in X-rays than spiral galaxies of similar optical magnitude.

Starburst galaxies have intense X-ray emission from a number of young supernova remnants and massive X-ray binaries. The X-ray luminosity of these blue galaxies is stronger than those of normal colour.

Galaxy clusters. Galaxy clusters are not just composed of galaxies, they also contain hot gas. This gas, which constitutes about 15% of a cluster's mass, forms a sphere sitting at the center of the cluster The temperature of the gas is very high, ranging from 0.2 keV to 10 keV. With such a high temperature, the gas is almost fully ionized, with the few electrons that are bound clinging to heavier ions such as iron. The dominant radiative process is bremsstrahlung emission.

1.2 High mass X-ray binaries

A High-Mass X-ray Binary (HMXB) is a binary star system in which the normal stellar component is a massive star: usually an O or B star. The companions have radii 10-30 $R_\odot$ ((almost) fill their critical Roche-lobes) and have masses larger than $10M_\odot$. The compact, X-ray emitting, component is generally a neutron star, black hole, or possibly a white dwarf. A fraction of the stellar wind of the massive normal star is captured by the compact object, and produces X-rays as it falls onto the compact object. In a high-mass X-ray binary, the massive star dominates the emission of optical light, while the compact object is the dominant source of X-rays. The massive stars are very luminous and therefore easily detected. HMXBs are located along the Galactic plane among their OB-type progenitor stars.

A separate sub-class of HMXBs is the Be-star X-ray binaries (first recognized as a class by Maraschi, Treves & van den Heuvel in 1976). The

Be-stars are deep inside their Roche-lobes, as is indicated by their generally long orbital periods ($\sim$ 15 days) and by the absence of X-ray eclipses and of ellipsoidal light variations. According to the luminosities and spectral types, the companion stars have masses in the range about $8 - 20 M_{\odot}$. The X-ray emission from the Be-star X-ray systems tends to be extremely variable.

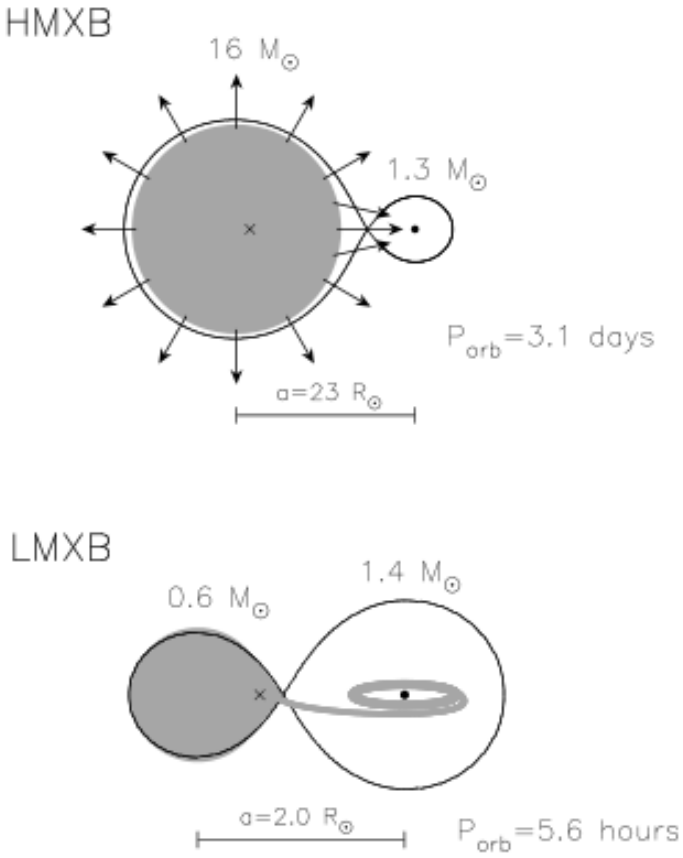

Figure 2: Examples of a typical HMXB (top) and LMXB (bottom). The neutron star in the HMXB is fed by a strong stellar wind and/or by atmospheric Roche-lobe overflow. The neutron star in an LMXB is fed by Roche-lobe overflow through an accretion disk (Tauris et al. (2003)).

1.3 Low mass X-ray binaries

A Low-Mass X-ray Binary (LMXB) is a binary system where one of the components is either a black hole or neutron star. The donor usually fills its

Roche lobe and therefore transfers mass to the compact star. The donor is less massive than the compact object, and can be on the main sequence, a degenerate dwarf (white dwarf), or an evolved star (red giant).

A typical low-mass X-ray binary emits almost all of its radiation in X-rays, and only in the few widest of these systems one can observe the spectrum of the optical companion. Most of the LMXBs are located in the Galactic bulge and in globular clusters, and thus appear to belong to an old stellar population. The apparent magnitude is typically around 15 to 20. The brightest part of the system is the accretion disk around the compact object. The orbital periods of LMXBs range from 11 minutes to 17 days.

Table 1: Main classes of Galactic X-ray sources.

	HMXB	LMXB
X-ray spectra	kT $\geq$ 15keV (hard)	kT $\leq$ 10keV (soft)
Type of time variability	regular X-ray pulsations, no X-ray bursts	only a few pulsars, often X-ray burst
Accretion process	wind (or atmospheric RLO)	Roche-lobe overflow
Timescale of accretion	10^5 yr	10^7-10^9 yr
Spatial distribution	Galactic plane	Galactic center and spread around the plane
Stellar population	young, age $<10^8$ yr	old, age $>10^9$ yr
Companion stars	early-type O, B stars (Pop.I), $> 10M_\odot$	blue stars (Pop. I and II) $< 1M_\odot$
L_{opt}/L_x	luminous, > 1	faint, $\ll 0.1$

1.4 Ultra-luminous X-ray sources

A general description defines the Ultra-luminous X-ray sources (ULXs) as those binaries whose luminosities are higher than what is expected for an accreting system hosting a stellar mass black hole ($M_{BH} \simeq 10M_\odot$).

If the source is powered by accretion and if the accretion is steady and spherically symmetrical, there is a limiting luminosity, L_{Edd}, for which the gravitational force inwards equals the radiation pressure outwards. For fully ionized hydrogen it is:

$$L_{Edd} = \frac{4\pi G M_{BH} m_p}{\sigma_T} \simeq 1.3 \times 10^{38} \frac{M_{BH}}{M_\odot} \quad (1)$$

where σ_T is the Thomson cross section, M_{BH} is the mass of the accreting object and m_p is the proton mass. For a stellar black hole of 10 $M_\odot$, the Ed-

dington luminosity is $\sim 1.3 \times 10^{39}$ erg/sec. Therefore, a more formal definition of ULXs is, off-nuclear, point-like sources in galaxies with X-ray luminosity in excess of 10^{39} erg/sec.

ULXs were first detected with Einstein Observatory (Long & Van Speybroeck, 1983). Their luminosity was significantly in excess of the Eddington limit of a neutron star ($\sim 2 \times 10^{38}$ erg/sec), suggesting accreting objects with masses of 100 $M_\odot$ or larger. Studying the X-ray Luminosity Function (XLF) of HMXBs, the ULXs reprecent the high luminosity tail of the XLF (Gilfanov, Grimm & Sunyaev, 2004). This suggests that ULXs may represent a high accretion stage of X-ray binaries, or also they could be binaries that include massive black holes, or beamed sources. Colbert et al. (2004) reported that these objects are found at a rate of only 1-2 per galaxy based on pointed X-ray observations.

There are 2 recent calatogs of ULXs relying on ROSAT (Liu & Bregman, 2005) and Chandra (Swartz et al., 2004) observations. Swartz et al. found 154 ULXs in 82 galaxies confirming their association with young stellar populations, especially those of merging and colliding galaxies. A significant fraction of ULXs are supernovae interacting with the circumstellar medium ($\sim$22%) or background AGNs ($\sim$25%). In the ROSAT survey, Liu & Bregman found 106 ULXs in 313 galaxies, showing also a strong connection of ULXs with star formation.

1.4.1 Why are ULXs so interesting?

In order to justify these super-Eddington luminosities, masses that exceed those of stellar black holes in binaries ($\sim$ 30 $M_\odot$ at moderate metallicity (Belczynski et al., 2010)) are required. ULXs could then be a new class of astrophysical objects, possibly unconnected with the evolution of the normal stellar population of a galaxy. They could fill the gap between stellar black holes and the supermassive black holes found in the nuclei of galaxies, forming a new category of black holes, called Intermediate Mass Black Holes (IMBHs). If ULXs host IMBHs then a lot of questions arise, such as how they formed, how these black holes are fueled. Some theories propose the formation of IMBHs in cosmological epochs (e.g. Niemeyer & Jedamzik, 1999) or in zero metallicity environments with the first generation of stars (Madau & Rees, 2001). In other scenarios, IMBHs were also predicted to occur at the center of young dense stellar clusters through the merging of smaller mass black holes (Bahcall & Ostriker, 1975) and, at the present time, this seems to be a very promising possibility for at least the brightest ULXs (Portegies Zwart et al., 2004).

On the other hand, ULXs could represent a particularly high-accretion

stage of X-ray binaries, possibly with a stellar black-hole accretor (King et al., 2001), or even be powered by relativistic jets, as in Doppler-beamed microquasars (Koerding, Falke & Markoff, 2002).

Since our knowledge for these objects is not yet satisfactory, it is important to study them more accurately.

1.4.2 Models of ULXs

The dominant models for the structure of ULXs are two:

Beaming model. In the beaming scenario, the black hole accrets mass from a companion star and the accretion disk around the black hole has a much more lower scattering optical depth over a restricted range of solid angles (beaming factor b, $b = \Omega/4\pi$) due to a central funnel. The X-ray emission is required to be in the direction of the observer. In this case the emitted luminosity is:

$$L = bL_{iso} = 10^{40} bL_{40}\ erg/sec \tag{2}$$

where L_{iso} is the isotropic luminosity and L_{40}=$L_{iso}/10^{40}$ erg/sec. Assuming that the source does not exceed the Eddington limit, the minimum black hole mass becomes:

$$M_{BH} \geq 10^2 bL_{40} M_{\odot} \tag{3}$$

Mild beaming ($b \simeq 0.1$) would require a minimum accretor mass of $10M_{\odot}$ that is commonly found in X-ray binaries for an observed L_x $\sim 10^{38}$ erg/sec. This model suggests that ULXs represent a short-lived phase of HMXBs probably during thermal-timescale mass transfer that lasts $\sim 10^5$ yr (King et al., 2001). This phase occurs in any Roche-lobe-filling binary when the donor star has a radiative envelope, or when it is more massive than the companion or/and fills the Roche lobe while expanding to the red giant stage, producing extremely high mass transfer rates.

Consequently, since ULXs descent from HMXBs, they are related to young stellar populations. The fact that the X-ray spectra of ULXs is similar to those of Galactic black hole systems, supports this type of model.

However, the beamed X-ray binary interpretation can not explain why several ULXs show a very high luminosity and, at the same time, a very low temperature of the accretion disk. The beaming factor (b $\sim$ 0.1) is difficult to be achieved with pure disk models, but they may require thicker disks with central funnels, called slim discs. Some X-ray binaries could be explained by a coupled disk/jet model, whose emission would naturally be relativistically

beamed. Such microquasar-like objects could be hosted in nearby galaxies (Mirabel & Rodriguez, 1999)

Intermediate-mass black holes. A companion star accrets material onto an IMBH ($> 100\ M_{\odot}$) that is light enough not to sink to the center of its host galaxy by dynamical friction, but sufficiently massive to be able to emit as ULX. The high mass of the black hole is consistent with isotropic emission (b=1) and no super-Eddington accretion is required. The IMBH interpretation offers a direct explanation of both the very high luminosity and low disk temperature of ULXs (Miller et al. 2004).

However, the major problem of the IMBH scenario for ULXs is the issue about the formation of such massive objects. These massive black holes could originate from the first generation of stars (Population III) at the early universe. By definition, the Population III stars evolved in an environment with negligible metallicity and their initial mass may be significantly larger than it is currently. Moreover, at zero-metallicity, winds and pulsations are negligible, so a star loses little of its mass during its evolution leaving a higher mass remnant.

In addition, a $\sim 100 M_{\odot}$ black hole may be produced in dense clusters through the merger of lower mass black holes, as in the ULX found in the central region of M82 galaxy (Matsushita et al., 2000) or by merging of stars in the cluster, causing a direct collapse into an IMBH. The ULX then may form by gaining a stellar companion by dynamical process.

On the other hand, it is difficult to explain how massive black holes could form in young stellar clusters further from the galactic nuclei, as in the Antennae galaxies (Zezas & Fabbiano, 2002) since most of the Antennae ULXs are displaced from their parent clusters suggesting that they have received kicks when their progenitor had a supernova explosion.

1.5 Extremely Metal Poor Galaxies

Extremely metal-poor galaxies (XMPGs) are very rare: they are fewer than 1% of dwarf galaxies, with a gas-phase oxygen abundance $log(O/H) + 12 \leq 7.65$ (Kunth & Ostlin 2000), or Z<5% solar metallicity. These galaxies are experiencing their first burst of star formation (e.g. Thuan, Isotov & Lipovetsky, 1997) and are mostly gas-rich, Blue Compact Galaxies (BCGs) with spectra dominated by emission lines.

The discovery of extragalactic objects with very low heavy element abundance was made by Searle and Sargent (1972) who reported the properties of two such galaxies: IZw18 and IIZw40. Dwarf galaxies show slow evolution compared to giant galaxies because of smaller mass densities, which fits with the observation that dwarfs (except dwarf elliptical/spheroidal) are more gas-

rich than giants. The lack of metal abundance in dwarfs can be explained because they have weaker gravitational potential hence are more susceptible to lose metal enriched material from supernova winds. Therefore, if we want to study the properties of XMPGs, we have to focus on dwarf galaxies. In particular, it is more convenient to focus on Blue Compact Galaxies because they are easier to discover and to derive their metallicity from their bright emission lines.

XMPGs are very important to study for understanding primeval galaxies, i.e. young systems undergoing their first burst of star formation. Since it is difficult to observe such objects at high redshifts because of their faintness, we can look for nearby galaxies with the same characteristics. The best such candidates are the XMPGs. Even though they have formed stars in the past, XMPGs are generating stars in almost pristine gas. In addition, these systems are very important for understanding the formation of black holes and binaries in the early universe.

1.5.1 ULXs in Extremely Metal Poor Galaxies

Several authors have suggested that Ultra-luminous X-ray sources are found in dwarf galaxies in the local universe (Swartz, Soria & Tennant, 2008) and in low metallicity environments (Zampieri et al., 2010). In addition, there is evidence indicating that ULXs are formed from stars in metal poor gas (e.g. Soria et al., 2005; Liu, Bregman, Miller & Kaaret, 2007). Consequently, XMPGs is a logical place to find ULXs if they favor metal-poor systems.

The main argument for this theory is that massive stars at low metallicity environments lose less mass through winds than high metallicity stars ($\frac{dm}{dt} = Z^{0.85}$, Vink, de Koter & Lamers, 2001). Therefore, they leave higher mass compact objects following core collapse. Stellar winds from hot stars are accelerated by radiative line-driving. The driving mechanism of the winds is radiation pressure on spectral lines of metals. Higher metallicity implies more spectral lines, thus more transfer of momentum to the absorbing ions and stronger winds, and therefore, more mass loss for a star of a given luminosity and T_{eff}.

At solar metallicity the black hole remnant after a supernova explosion can reach at most $\sim 10M_{\odot}$ while for sub-solar metallicities is easier to produce high mass black holes. This happens because massive stars in low metallicities tend to retain their massive envelopes at the time of supernova explosion. The supernova shock wave loses a large amount of energy to unbind the envelope until the wave stops and the star collapses into a black hole. The maximum black hole mass obtained for moderate metallicity ($Z = 0.3Z_{\odot}$) is $M_{bh,max} = 30M_{\odot}$ while in the very low metallicity environment the

maximum black hole mass can be as high as $M_{bh,max} = 80\ M_{\odot}$ ($Z = 0.01 Z_{\odot}$) (Belczynski et al. 2010). These black holes can radiate at higher luminosities without violating the Eddington limit, explaining isotropic luminosities of $\sim 10^{40}$ erg/sec. The formation of these massive black holes does not require an exotic mechanism as it is the result of stellar evolution. For very bright ULXs ($\leq 10^{40}$ erg/sec) only modest beaming or slight violations of the Eddington limit are required.

Therefore, ULXs formed in low metallicity environments can explain the super-Eddington luminosities with the simple mechanism of star formation. Only modest beaming is required to justify the bright ULXs. However, this model requires a slowly rotating star to prevent mass loss.

2 X-ray data analysis

2.1 Galaxy sample

We are interested in studying the population of ULXs in a sample of 25 extremely metal poor galaxies in the local universe (d≤50 Mpc). These are the most metal-deficient galaxies known. Most of those are BCD galaxies. The distances of the galaxy sample range from 3.1-52.6 Mpc. Three galaxies in the sample have already been observed (archival data) with Chandra telescope (I Zw18, SBS 0335-052, SBS 0335-052W) and it has been found that each of them contains ULXs (Thuan, Bauer, Papaderos & Isotov, 2004). The other galaxies have been observed between 30/08/2009 and 23/08/2010 and their Chandra X-ray data have not been processed previously. The exposure times of the galaxies are between 5-60 ksec. In Table 2 the basic properties of the galaxy sample are presented and the parameters of the observation are listed in Table 3.

2.2 The Chandra Mission

The Chandra X-ray Observatory (CXO) is a satellite launched by NASA on July 23, 1999. It was named in honor of the Indian-American physicist Subrahmanyan Chandrasekhar. Prior to its successful launch, the Chandra Observatory was known as AXAF, the Advanced X-ray Astrophysics Facility. Chandra is sensitive to X-ray sources 100 times fainter than any previous X-ray telescope, due primarily to the high angular resolution of its mirrors. Chandra has been returning data since the month after it launched. It is operated by the Chandra X-ray Center at the Smithsonian Astrophysical Observatory (SAO) in Cambridge, Massachusetts, with assistance from the Massachusetts Institute of Technology (MIT) and Northrop Grumman Space Technology.

The orbit of Chandra is highly elliptical with period about 63.5 hours. The Chandra spacecraft spends approximately 85% of its orbit above the van Allen belts and makes uninterrupted observations of as long as 55 hours.

The Observatory has three major parts: the X-ray telescope, whose mirrors focus X-rays from celestial objects; the science instruments which record

Table 2: The Extremely Metal Poor Galaxy sample.

Galaxy	R.A. (J2000)	Dec. (J2000)	Distance (Mpc)	D_{25} (arcmin)	N_H (10^{20} cm^{-2})	12+log(O/H)
UGC 772	08h25m55.5s	+35d32m32s	3.10	1.20×0.90	11.5	7.24±0.03
SDSS J210455.31-003522.2	21h04m55.3s	-00d35m22s	13.7	-	6.47	7.26±0.03
SBS 1129+576	11h32m02.5s	+57d22m46s	26.3	0.75×0.10	0.87	7.41±0.07
HS 0822+3542	08d25m55.5s	+35d32m32s	12.7	0.27×0.12	4.82	7.35
SDSS J120122.32+021108.5	12h01m22.3s	+02d11m08s	18.4	0.35×0.12	1.88	7.55±0.03
RC2 A1116+51	11h19m34.3s	+51d30m12s	20.8	0.24×0.17	1.19	7.51±0.04
SBS 0940+544	09h44m16.6s	+54d11m34s	24.7	1.22×1.54	1.34	7.48
KUG 1013+381	10h16m24.5s	+37d54m46s	19.6	0.38×0.25	1.41	7.58
SBS 1415+437	14h17m01.4s	+43d30m05s	10.4	0.75×0.15	1.21	7.60
6dF J0405204-364859	04h05m20.3s	-36d49m01s	11.0	0.48×0.35	0.88	-
SDSS J141454.13-020822.9	14h14m54.1s	-02d08m23s	24.6	0.34×0.24	4.17	7.32
SDSS J223036.79-000636.9	22h30m36.8s	-00d06m37s	18.0	0.24×0.20	5.20	7.64
UGCA 292	12h38m40.0s	+32d46m01s	7.8	1.00×0.70	1.34	7.27±0.08
HS 1442+4250	14h44m12.8s	+42d37m44s	10.5	1.13×0.26	1.53	7.63
KUG 0201-103	02h04m25.6s	-10d09m35s	22.7	0.46×0.19	2.08	7.56
SDSS J081239.52+483645.3	08h12m39.5s	+48d36m45s	9.04	0.46×0.23	4.58	7.16
SDSS J085946.92+392305.6	08h59m46.9s	+39d23m06s	10.9	0.39×0.27	2.44	7.45
KUG 0743+513	07h47m32.1s	+51d11m28s	8.6	0.70×0.30	5.17	7.68
KUG 0937+298	09h40m12.8s	+29d35m30s	11.2	0.62×0.23	1.87	7.45
KUG 0942+551	09h46m22.8s	+54d52m08s	24.4	0.37×0.18	1.23	7.66
SBS 1102+606	11h05m53.7s	+60d22m29s	19.9	0.60×0.28	0.59	7.64±0.04
RC2 A1228+12	12h30m48.5s	+12d02m42s	21.2	0.29×0.16	2.47	7.64
I Zw 18	09h34m02.0s	+55d14m28s	17.1	0.30×0.20	1.99	7.17
SBS 0335-052	03h37m44.0s	-05d02m40s	52.6	0.23×0.20	4.98	7.25±0.05
SBS 0335-052W	03h37m38.4×s	-05d02m37s	52.2	0.10×0.13	4.96	7.10±0.08

NOTES: Distances are taken from the NASA/IPAC Extragalactic Database (NED). D_{25} shows the diameter of major×minor axis. The Galactic N_H is calculated with Colden tool, http://cxc.harvard.edu/toolkit/colden.jsp. Metallicities are taken from literature. For the galaxy SDSS J210455.31-003522.2 we used the optical diameter from NASA/SAO Image Archive.

the X-rays so that X-ray images can be produced and analyzed; and the spacecraft, which provides the environment necessary for the telescope and the instruments to work.

The X-ray telescope. The Chandra X-ray telescope consists of 4 pairs of concentric thin-walled, grazing-incidence Wolter Type-I mirrors called the High Resolution Mirror Assembly (HRMA). The front mirror of each pair is a paraboloid and the back a hyperboloid. The eight mirrors were fabricated from Zerodur glass, polished, and coated with iridium on a binding layer of chromium. The X-rays are reflected from the surface of the mirrors if the angle of incidence is large which means that the angles between the surface

Table 3: X-ray observation characteristics.

Galaxy	Obs.ID	Date	Exposure (sec)	Instrument
UGC 772	11281	30-08-2009	5081	ACIS-S3
SDSS J210455.31-003522.2	11282	04-09-2009	5007	ACIS-S3
SBS 1129+576	11283	06-07-2010	14755	ACIS-S3
HS 0822+3542	11284	20-12-2009	51200	ACIS-S3
SDSS J120122.32+021108.5	11286	23-11-2009	8097	ACIS-S3
RC2 A1116+51	11287	07-11-2009	11640	ACIS-S3
SBS 0940+544	11288	18-01-2010	16828	ACIS-S3
KUG 1013+381	11289	24-01-2010	9402	ACIS-S3
SBS 1415+437	11291	30-102009	5114	ACIS-S3
6dF J0405204-364859	11292	28-05-2010	5010	ACIS-S3
SDSS J141454.13-020822.9	11293	18-12-2009	16680	ACIS-S3
SDSS J223036.79-000636.9	11294	25-09-2009	7715	ACIS-S3
UGCA 292	11295	06-11-2009	5007	ACIS-S3
HS 1442+4250	11296	26-11-2009	5188	ACIS-S3
KUG 0201-103	11297	06-09-2009	13590	ACIS-S3
SDSS J081239.52+483645.3	11298	18-12-2009	4777	ACIS-S3
SDSS J085946.92+392305.6	11299	18-12-2009	4782	ACIS-S3
KUG 0743+513	11300	18-12-2009	5073	ACIS-S3
KUG 0937+298	11301	16-01-2010	5007	ACIS-S3
KUG 0942+551	11302	19-01-2010	16020	ACIS-S3
SBS 1102+606	11285	23-08-2010	10340	ACIS-S3
RC2 A1228+12	11290	26-07-2010	12200	ACIS-S3
I Zw 18	805	08-02-2000	40750	ACIS-S3
SBS 0335-052	796	07-09-2000	59742	ACIS-I3
SBS 0335-052W	796	07-09-2000	59742	ACIS-I3

and the direction of the incident photon are a few degrees. Therefore, to focus the X-rays from a source, a parabolic reflector is used together with a hyperbolic to shorten the focal length. The nested shells of the telescope are increasing the collecting area. HRMA produces images of the point spread function (PSF) of <0.5 arcsec.

The science instruments/ACIS. The most important instruments are the Advanced CCD Imaging Spectrometer (ACIS), the High Resolution Camera (HRC), the High-Energy Transmission Grating (HETG) and the Low Energy Transmission Grating (LETG). In this work, the basic instrument of observation is ACIS. ACIS is comprised of two CCD arrays, a 4-chip array, ACIS-I; and a 6-chip array, ACIS-S. The CCDs are composed of silicon. Each

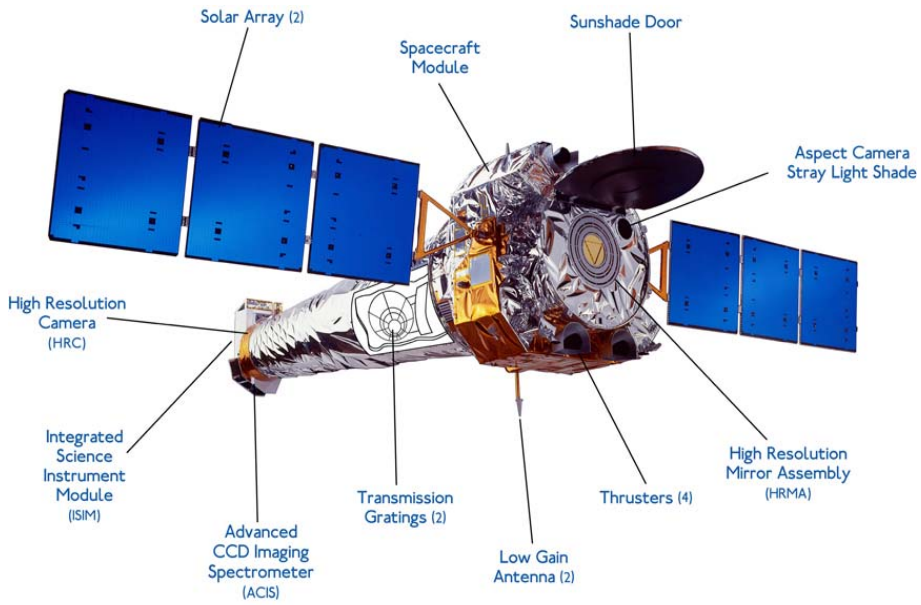

Figure 3: The Chandra Observatory with certain sub-systems labeled.

CCD has size of 1024×1024 pixels. The spatial resolution for on-axis imaging with HRMA/ACIS is one pixel corresponding to 24.0 μm^2 $\sim$ 0.492 arcsec. Approximately 90% of the encircled energy of a point source lies within 4 pixels (2 arcsec radius) at 1.49 keV and within 5 pixels (2.5 arcsec radius) at 6.4 keV. The camera's operating temperature is between -90°C to -120°C. We summarize the ACIS characteristics to Table 2.

Table 4: Main characteristics of the ACIS

Energy range	0.1-1.0 keV
CCD format	1024 by 1024 pixels
Pixel size	23.985 microns (0.492±0.0001 arcsec)
On-axis effective Area	110 cm^2 @ 0.5 keV (FI)
(integrated over the PSF to	600 cm^2 @ 1.5 keV (FI)
$>$ 99 encircled energy)	40 cm^2 @ 8.0 keV (FI)
Point-source sensitivity	4x10^{-15} ergs/sec/cm^2 in 10^4 sec (0.4-6.0 keV)
System noise	$<$ $\sim$2 electrons (rms) per pixel
Detector operating temperature	-90° C to -120° C

The spacecraft. The spacecraft system provides the support structure and environment necessary for the telescope and the science instruments to work as an observatory. The size of Chandra is 13.8m long with 4.2m

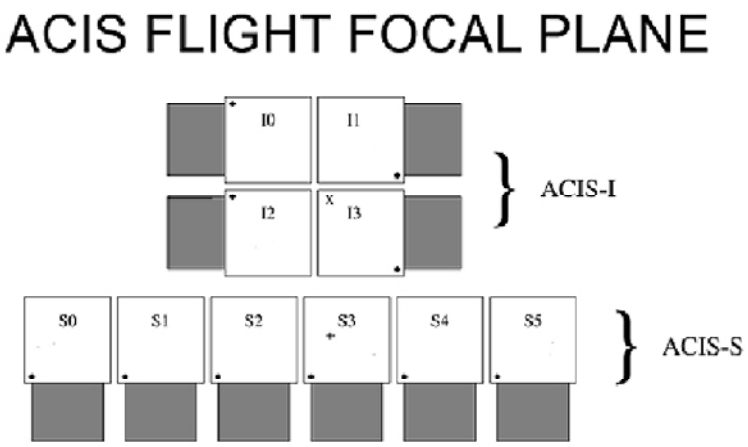

Figure 4: A schematic drawing of the 2 CCD arrays of ACIS: a 4-chip array, ACIS-I, with front-illuminated (FI) CCDs and a 6-chip array, ACIS-S, with 4 FI and 2 back-illuminated (BI) CCDs.

diameter and its weight is about 4,800kg.

The Pointing Control and Aspect Determination (PCAD) controls the pointing and dithering of the observatory and provides the data from which both the relative and absolute aspect are determined. Chandra's electrical power comes from its solar arrays. The solar arrays generate approximately 2 kW of power which is stored in 3 banks of batteries and distributed to the heaters, science instruments, computers, transmitters, etc. Two 1.8 Gbit solid state recorders could store 18.8 hours of data per recorder. In order to provide motion to the observatory, Chandra has two different sets of thrusters: one for propulsion and the other for momentum unloading. The propulsion thrusters were used immediately after launch to help propel Chandra into its final orbit, which is elliptical and very high in altitude. The momentum unloading thrusters are periodically used to apply torques to Chandra and, thereby, lower the accumulated momentum in its reaction wheels, which are used to control Chandra's attitude. Chandra's thermal control system consists of a cooling radiator, insulators, heaters and thermostats.

Chandra has two low gain antennae, either one of which may be used for two-way communications with Chandra's Operations Control Center (OCC).

2.3 X-Ray data reduction

We have acquired data from Chandra Data Archive[1] for a sample of 25 galaxies and processed these datasets in order to measure the luminosity of the sources (if any) in these galaxies and classify them as ULXs.

All observations were made with the back-illuminated chip ACIS-S3 except for the galaxies SBS 0335-052 and SBS 0335-052W, which were observed with the front-illuminated ACIS-I3 camera. The observations were performed in VFAINT mode, since the sources were very weak and extended, in order to reduce the background using the information from 5x5 pixel islands, apart from I Zw18 (FAINT mode: 3x3 pixel island).

The initial processing of the raw data was carried out with the Chandra Interactive Analysis of Observations software (CIAO), version 4.2 and the CALibration DataBase (CALDB), version 4.3.0. The raw data before their distribution first follow the Standard Data Processing (SDP), or 'pipeline' processing[2]. We reprocess the 'event 1' files of the data sets that contain photon event data of the observation stored as a multi-dimensional array of pixel location, time of the event, energy using the `acis_process_events` tool. With this tool a 'new event 1' file is created so we can reconstruct the X-ray images. In this latest version of the processing software, it has already been applied the cosmic ray afterglow correction, which means that any residual from the interaction of a cosmic ray in the CCD is subtracted. The basic corrections of the 'event 1' files are listed below.

Bad pixel correction. We use the default bad pixel file which contains that have an unusually large number of events during an observation (hot pixels). The number of bad pixels is affected by the temperature of the CCD (normal temperature is -120°C). This option will mark the bad pixels in the 'event 1' file.

Charge Transfer Inefficiency. The charge that is deposited on the CCD is moved to the readout and during this transfer charge can be lost as it is shifted from one pixel to the next, due to states in the lattice, called 'traps' which retain part of the charge and cause less charge to be read out than the amount of charge deposited. These traps are causing loss of spectral resolution and sensitivity. Due to the accumulated effects of cosmic radiation damage, the Charge Transfer Inefficiency (CTI) on the CCDs is increasing with time. The tool `acis_process_events` includes a CTI adjustment procedure that corrects for most of such effects. The `acis_process_events` tool has an algorithm to estimate the amount of charge deposited on a CCD for an event from the amount of charge read out and the location of the event

[1] http://cda.harvard.edu/chaser/

[2] See http://cxc.harvard.edu/ciao/threads/data.html

on the detector.

Time-dependent gain. The gain of a CCD camera is the number of digital units, or else, counts, contained in each pixel of the CCD image that derive from the number of electrons recorded by the CCD. The time-dependent gain (TGAIN) adjustment is necessary because as the CTI increases with time, the 'effective gains' of the detector are drifting. The size of the adjustment is a function of time, location and pulse-height (charge per pixel) of an event. The tool `acis_process_events` includes a TGAIN adjustment.

Very faint mode. In ACIS very faint (VFAINT) mode for very faint observed sources, there is a 5x5 pixel event island, instead of just a 3x3 as in FAINT mode. The `acis_process_events` tool can use the pulse heights in the outer 16 pixels of the 5x5 event island to distinguish the good X-ray events from the bad events that are usually associated with cosmic rays, and have a better calculation of the background.

Aspect solution file. We input the aspect solution file that contains the sky coordinates of the telescope pointing during the observation to reconstruct the image from dither pattern.

2.3.1 Imaging

After the 'new event 1' file is created, we followed the filtering steps for ACIS imaging in order to create the final 'event 2' file. The CIAO tool used for this filtering is `dmcopy`. We filter the data for selecting events with the standard set of event grades 0, 2, 3, 4 and 6, ignoring the bad grades from cosmic rays. We also filter the 'new event 1' file with the exact start and stop times of the observation (Good Time Intervals, (GTI)). In order to save disk space, we trim the image to include only the CCD that covers the target of the observation (for our observations we use ccd_id=7, apart from two observations, SBS 0335-052 and SBS 0335-052W, where we use ccd_id=3). Finally, we chose the full energy band of 0.3-8.0 keV. With the 'event 2' file that is created the pipeline analysis is completed.

2.3.2 Source detection

The detection of X-ray sources on the images was carried out with the CIAO tool `wavdetect`. This tool is a wavelet-based source detection algorithm (Freeman et al., 2002) that correlates the image with 'Mexican Hat' wavelet functions of different scales (radii of the wavelet function) and then searches the results for significant correlations generating this way a source list.

We input the image from the 'event 2' file and run the `wavdetect` tool

in the energy band of 0.3-8.0keV. The wavelet scales that were applied were of 1.0, 2.0, 4.0, 8.0 and 16.0 pixels. We set a threshold significance for identifying a pixel as belonging to the source at 10^{-6}. After the detection is completed, a region file is created that includes all detected sources. From these sources, we keep only those that are within the D_{25} region, the elliptical contour best corresponding to the 25 mag arcsec^{-2} blue isophote, using data based on the Third Reference Catalog of galaxies (RC3) (de Vaucouleurs et al. 1991). The results of the source detection are show on Table 5.

Table 5: X-ray source detection.

Galaxy	Number of sources	Position R.A. (J2000) Dec. (J2000)
SBS 1129+576	1	11h32m02.57s +57d22m36.87s
RC2 A1116+51	1	11h19m34.13s +51d30m12.48s
SBS 0940+544	1	09h44m16.44s +54d11m34.39s
I ZW 18	1	09h34m01.97s +55d14m28.23s
SBS 0335-052	1	03h37m44.04s -05d02m39.89s
SBS 0335-052W	1	03h37m38.44s -05d02m37.14s

2.3.3 Photometry

Based on the `wavdetect` source list, the source regions were defined. We also create the corresponding background regions by setting apertures with larger radii than the sources. We perform photometry for these sources, using the `dmextract` tool. The results of the photometry are shown at Table 6. The source counts per pixel follow the Poisson distribution and the count error, since the number of counts is very low, the Gehrels approximation: error $= 1 + \sqrt{(N + 0.75)}$ (Gehrels et al. 1989).

Finally, Figures 4-9 show the galaxies that host X-ray sources in the 0.3-8.0 keV band. The red ellipses depict the X-ray sources and the green the D_{25} regions of the galaxies. In the following sections, we will calculate the luminosity of these sources and classify them as possible ULX candidates.

2.4 Spectral Analysis

We are able now to extract the spectra of the sources. We extract the energy channels (Pulse Invariance, PI) from the region of the source of the 'event 2' file using the CIAO tool `dmextract` and bin them to a histogram

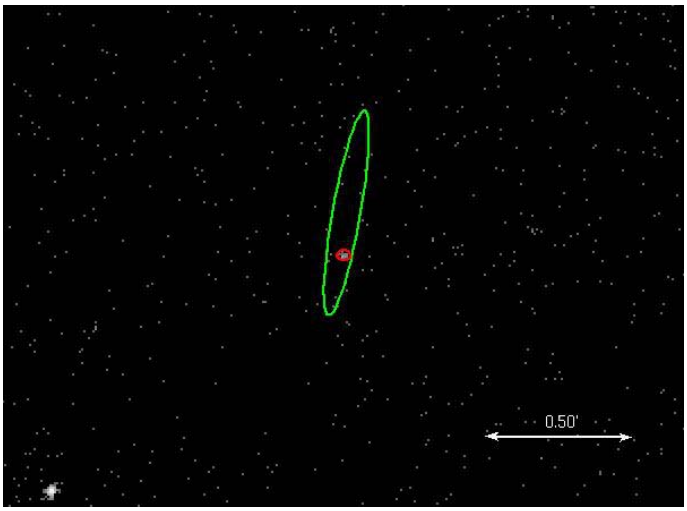

Figure 5: X-ray image of SBS 1129+576 in the 0.3-8.0 keV band.

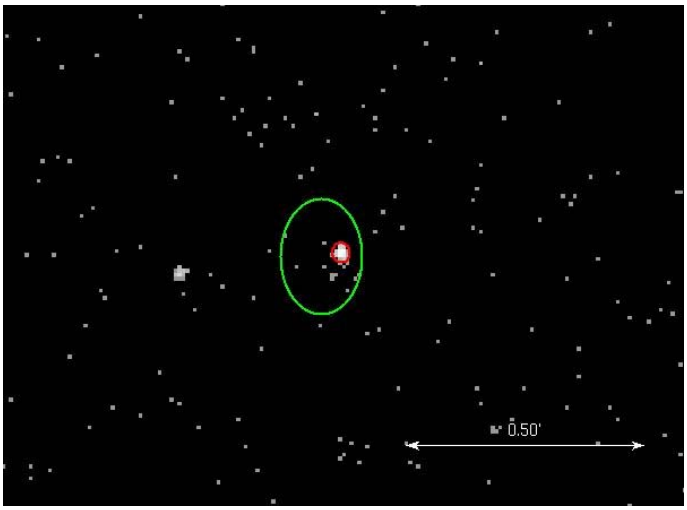

Figure 6: X-ray image of [RC2]A1116+51 in the 0.3-8.0 keV band.

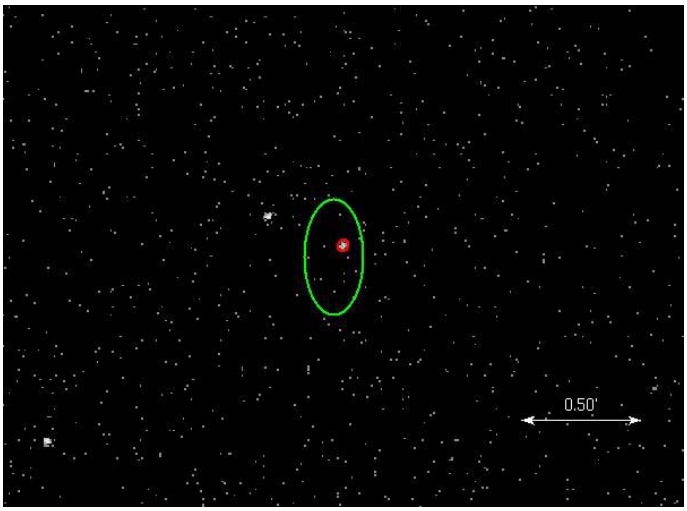

Figure 7: X-ray image of SBS 0940+544 in the 0.3-8.0 keV band.

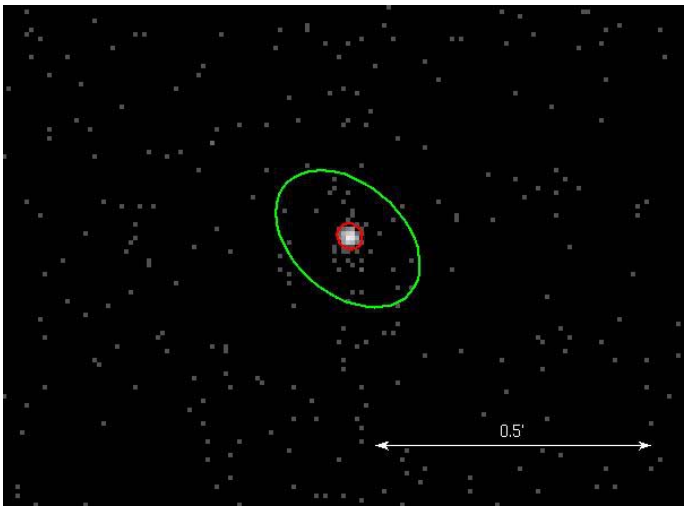

Figure 8: X-ray image of IZw18 in the 0.3-8.0 keV band.

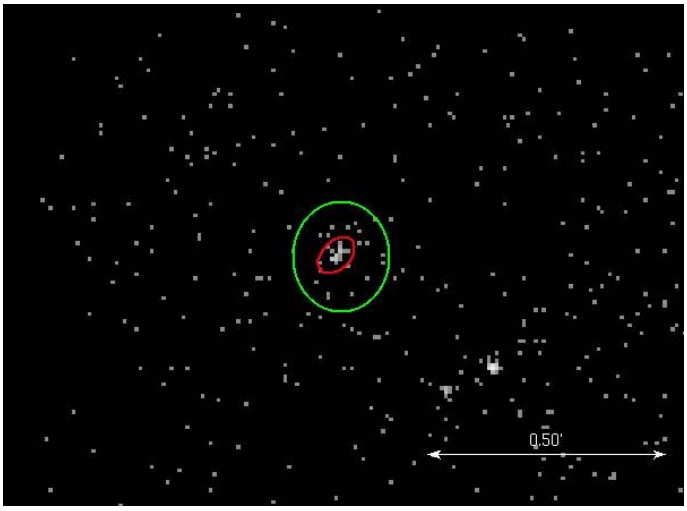

Figure 9: X-ray image of SBS 0335-052 in the 0.3-8.0 keV band.

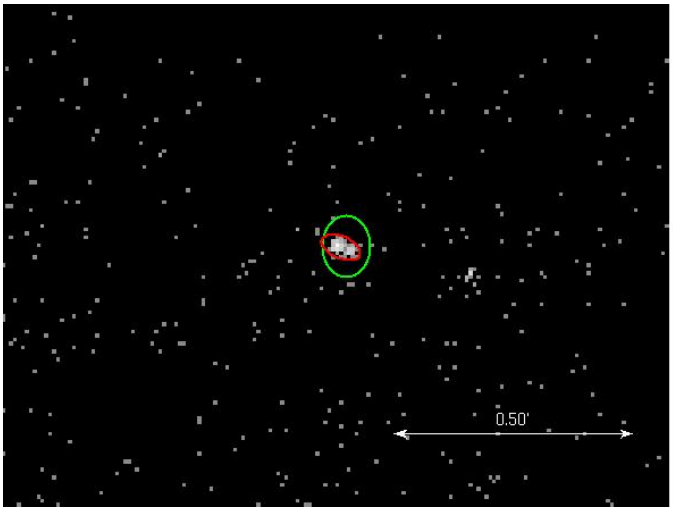

Figure 10: X-ray image of SBS 0335-052W in the 0.3-8.0 keV band.

Table 6: Measurements of the X-ray sources.

Galaxy	Net counts	Background counts
SBS 1129+576	21.47±5.71	0.19±1.97
RC2 A1116+51	89.04±10.48	0.21±1.98
SBS 0940+544	39.20±7.32	0.20±1.97
I ZW 18	494.44±23.25	1.56±2.51
SBS 0335-052	28.21±6.38	1.30±2.43
SBS 0335-052W	116.29±11.82	1.30±2.43

table file. We do the same for the corresponding background region. These files contain the observed source and background counts in each PI channel.

When we measure the spectrum of a source using a spectrometer, such as ACIS, what it obtains is not the actual spectrum, but the photon counts within the instrument energy channels or more precisely, the pulse invariant. The conversion between the PI channels and the energy is roughly: PI=[(energy/14.6eV)+1]. This observed spectrum is related to the actual spectrum of the source, f(E), with the following equation:

$$C(E, PI) = \int RMF(E/PI) \cdot ARF(E) \cdot f(E) dt d(PI), \qquad (4)$$

where C is the number of counts, RMF is the Response Matrix File, ARF is the Auxiliary Response File and dt the exposure time.

Response Matrix File (RMF). The Response Matrix File (RMF) is proportional to the probability of the incoming photon of a certain energy, E, to be detected into a channel, PI, of the CCD. Since CCD detectors are not perfect, this indicates a spread of the recorded energy of the observed counts by the detector's resolution. This energy-channel mapping is stored in the form of a 2-D matrix and in CCD detectors, as ACIS, this matrix is almost diagonal.

The tool to generate the RMF is `mkacisrmf`[3] which calculates the RMF by tabulated ACIS response calibration information. The response of the detector is a function of position on the CCD. To construct the RMFs for a source region, `mkacisrmf` sums the response function of each pixel over the source region, weighted by an image of the field in CCD detector coordinates, a weights map (WMAP) file. The RMF is calculated on energy grids that range from 0.3 to 9.5 keV in 5 eV increments and on PI channels. Figure 11 shows the ACIS RMF to be almost diagonal with a spread in energy due to flaws of the detector.

[3]See http://cxc.harvard.edu/ciao/threads/mkacisrmf

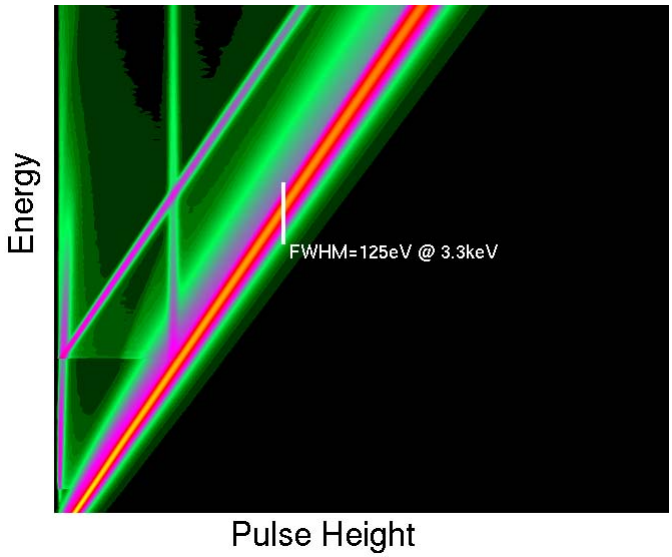

Figure 11: The ACIS RMF figure shows a spread in energy due to flaws of the detector.

Auxiliary Response File (ARF). The Auxiliary Response File (ARF) contains the combined detector's effective area and its quantum efficiency (QE) as a function of energy. The effective area and the QE are multiplied together to create the ARF, which gives the sensitivity of the detector in different energies.

The CIAO tool to create the ARF is `mkarf`[4]. The energy grid of the ARF is the same as the RMF. The input calibration data (detector quantum efficiencies, mirror effective areas, locations of bad pixels, etc.) are obtained from the calibration data library. The ARF is calculated at the source position (using the `dmstat` tool) on the CCD camera (ACIS-S3 or ACIS-I3).

2.5 Spectral fitting

The program that we used to fit the spectrum is XSPEC (version 12.6.0). As we mentioned before the real spectrum of the source is calculated by inverting equation (4):

$$C(E, PI) = \int RMF(E/PI) \cdot ARF(E) \cdot f(E) dtd(PI),$$

The problem is that in general, such inversions tend to be non-unique and unstable to small changes of the number of counts, C. XSPEC solves

[4]See http://cxc.harvard.edu/ciao/threads/pieces

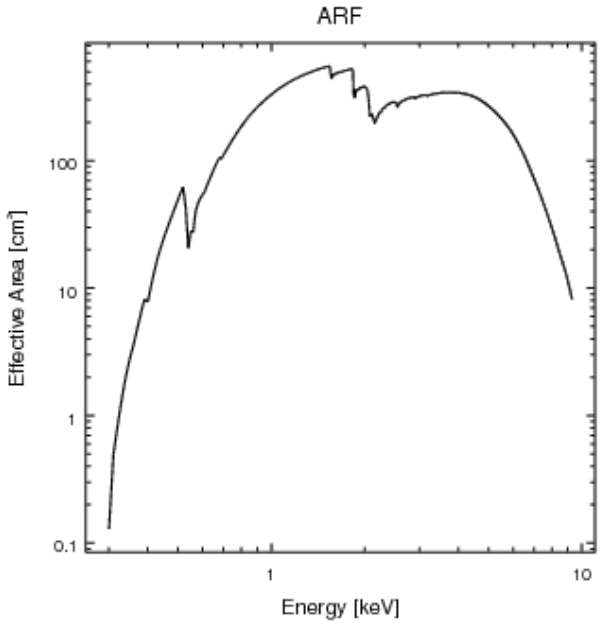

Figure 12: The ACIS ARF figure.

this problem by choosing a model spectrum, $f_m(E)$, that can be described in terms of a few parameters and fits it to the data.

To obtain the observed spectrum, C(E), XSPEC uses the data files of the source and the background files that were created previously, as well as the RMF and ARF, for every galaxy. The theoretical count spectrum, C_{th}, is compared to the observed data, C(E). Then, we implement a fit statistic between the two spectra to see how well the model spectrum fits the data obtained by the spectrometer. The model parameters then are varied to find the parameter values that give the most desirable fit statistic. The model spectrum, $f_m(E)$, corresponding to the best-fit parameters is considered to be the best-fit model. The fit statistic in use for determining the 'best-fit' model is χ^2.

The model spectrum for this analysis is assumed to be a power-law, absorbed by the Galactic column density, as given by equation (5). This is the most simple model to describe the spectrum of ULXs that gives empirically good fits and is characterized by a photon index from 1.5 to 2.0.

$$f_m(E) = Ne^{-\sigma(E)N_H} \cdot E^{-\Gamma}dE, \tag{5}$$

σ absorbion cross-section, N_H neutral hydrogen column density, Γ photon

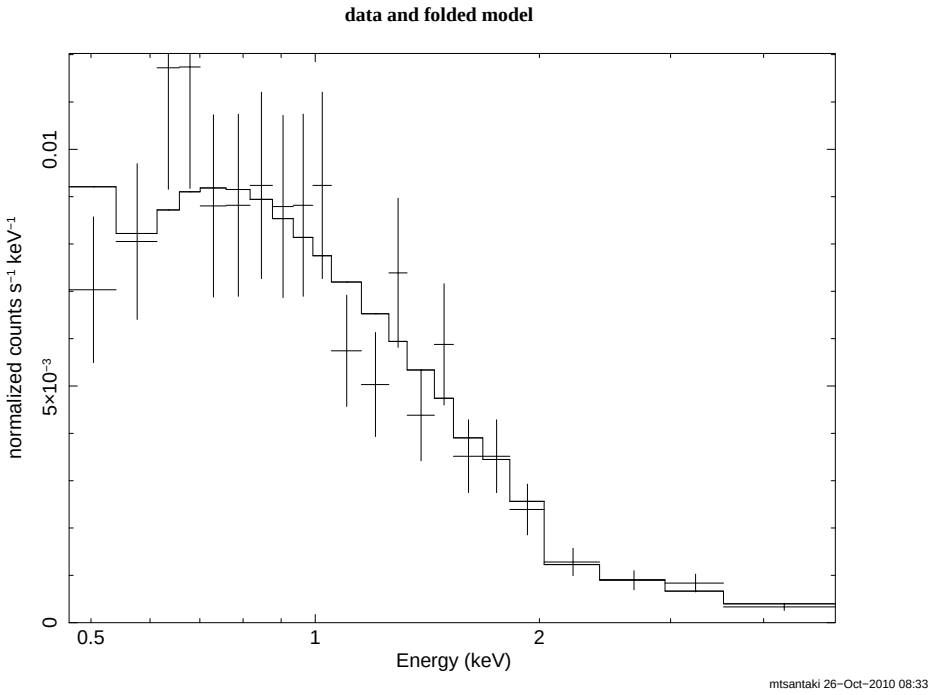

Figure 13: X-ray spectrum of IZw18 point source.

index, N normalization factor. The X-rays are absorbed by the Galactic Interstellar Medium (ISM), that is consisted mostly by hydrogen gas. The optical depth of the absorbion of the ISM is proportional to N_H. The Galactic line-of-sight N_H column density is calculated with Chandra Colden tool (Dickey & Lockman, 1990) (see Table 2).

The energy channels are binned in groups of at least 20 counts per group, in order to apply χ^2 statistics. The total flux in the energy band from 0.3 to 8.0 keV is calculated by the integral of the model.

Only one source, IZw18, had adequate number of counts to use this method. The spectrum of this source is best fit with a power law of 1.88 and N_H of 7.54×10^{20} cm^{-2}. Figure 13 shows the spectrum of I Zw 18 point source, the points are the observed data and the best fit model is with solid line in the energy band of 0.3-8.0 keV.

The remaining sources had too few counts for spectral fits. We estimate the count-rate and the flux that corresponds to the simulated model. We estimate their luminosities by calculating the count-rate to flux conversion factors. The results from the spectral fitting are listed at Table 7.

Then the conversion factor A is:

$$A = \frac{Flux}{CountRate}, [(erg/sec/cm^2)/(counts/sec)] \quad (6)$$

Table 7: Spectral fit results.

Galaxy	Source count-rate (counts/sec)	Γ	N_H (10^{20} cm^{-2})	χ^2/dof
I ZW 18	0.0111	$1.88^{+0.22}_{-0.20}$	$7.54^{+4.76}_{-6.17}$	12.69/19
SBS 1129+576	781.710	1.70	0.87	
RC2 A1116+51	777.725	1.70	1.19	
SBS 0940+544	774.579	1.70	1.34	
SBS 0335-052	472.695	1.70	4.98	
SBS 0335-052W	533.418	1.70	4.96	

NOTE: Only IZw18 had adequate data for spectral fitting. For the rest of the sources we used simulated data.

The actual flux of the source is calculated as a function of the net counts of the source and the exposure time of the observation, t.

$$F = A\frac{NetCounts}{t}, [erg/sec/cm^2] \quad (7)$$

Finally, the luminosity of each source is computed by the formula below and the results are listed at Table 8, using the different values of A for each galaxy.

$$L = F \cdot 4\pi D^2, [erg/sec]. \quad (8)$$

In Table 8 we show the flux and L_x of the detected sources. We conclude that all sources have luminosities above the Eddington limit, apart the source at SBS 1129+576 that is on the limit. These sources are classified as ULXs.

Table 8: X-ray emission from the sources.

Galaxy	Conversion Factor (10^{-12} erg/sec/cm^2/counts/sec)	Exposure time (sec)	Flux (10^{-15}erg/cm^2/sec)	L_x (10^{39}erg/sec)
SBS 1129+576	7.80	14755	1.14±0.30	0.72±0.19
RC2 A1116+51	7.75	11640	5.93±0.70	2.93±0.35
SBS 0940+544	7.79	16828	1.81±0.34	1.26±0.24
I ZW 18	6.15	25956	7.46±0.35	4.92±0.25
SBS 0335-052	11.84	59742	0.56±0.13	1.86±0.42
SBS 0335-052W	11.84	59742	2.31±0.23	7.53±0.77

NOTE: Fluxes and luminosities are calculated at the energy range 0.3-8.0 keV.

Since the flux to count-rate factor is almost the same for observations with the same camera and during the same period of time, we calculate it as the mean value of 4 galaxies. Therefore, we have for the ACIS-S:

A= $(7.37 \pm 0.16)\times10^{-12}$ [(erg/sec/cm^2)/(counts/sec)]
and for the ACIS-I:
A= 1.18×10^{-11} [(erg/sec/cm^2)/(counts/sec)].

2.6 Completeness

Apart from the sources we detected, there may be more faint sources that we were not able to detect due to inadequate exposure. We want to estimate the number of undetected sources above the 10^{39} ergs/sec limit by calculating the required threshold luminosities of all galaxies. The completeness limit is expressed by the source detection probability of a galaxy is a function of the source and background intensity, measured in counts. For example, 90% completeness means that we are confident that we have detected the 90% of the existing sources. The detection probability as a function of source counts and background counts/pixel can be parameterized by the following function (Zezas et al., 2007):

$$A(C) = 1.0 - \lambda_0 C^{-\lambda_1} e^{-\lambda_2 C} \tag{9}$$

where C is the source intensity in counts, λ_0, λ_1, λ_2 parameters that depend on the background counts per pixel.

All galaxies of our sample were measured to have background level below 0.025 counts per pixel. The best-fit parameters for this background give a detection probability of the form:

$$A(C) = 1.0 - 11.12 C^{-0.83} e^{-0.43C}. \tag{10}$$

Therefore, by solving the equation for 90% and 50% completeness, the corresponding source counts are: $C_{90} = 7.2$ counts and $C_{50} = 4.4$ counts.

Table 9 shows that all luminosities of 90% completeness and all luminosities 50% completeness, are well under the Eddington limit. This means that we have detected at least 90% of all existing ULX sources in the galaxy sample. The ones with no sources do not have ULXs.

Table 9: Completeness

Galaxy	Exposure time (sec)	90% (10^{38} erg/sec)	50% (10^{38} erg/sec)
UGC 772	5081	1.66	1.01
SDSS J210455.31-003522.2	5007	2.39	1.46
SBS 1129+576	14755	2.40	1.47
HS 0822+3542	5120	2.00	1.23
SDSS J120122.32+021108.5	8097	2.66	1.63
RC2 A1116+51	11640	2.37	1.45
SBS 0940+544	16828	2.31	1.41
KUG 1013+381	9402	2.60	1.59
SBS 1415+437	5114	1.35	0.82
6dF J0405204-364859	5010	1.54	0.94
SDSS J141454.13-020822.9	16680	2.31	1.41
SDSS J223036.79-000636.9	7715	2.67	1.63
UGCA 292	5007	0.08	0.05
HS 1442+4250	5188	1.35	0.83
KUG 0201-103	13590	2.41	1.47
SDSS J081239.52+483645.3	4777	1.09	0.67
SDSS J085946.92+392305.6	4782	1.58	0.97
KUG 0743+513	5073	0.93	0.57
KUG 0937+298	5007	1.59	0.97
KUG 0942+551	16020	2.36	1.45
SBS 1102+606	10340	2.44	1.49
RC2 A1228+12	12200	2.37	1.43
I ZW 18	25956	0.72	0.44
SBS 0335-052	59742	4.74	2.89
SBS 0335-052W	59742	4.66	2.85

3 IR data analysis

3.1 Spitzer space telescope

The Spitzer Space Telescope (SST), formerly the Space Infrared Telescope Facility (SIRTF) is an infrared space observatory launched in 2003. Spitzer is the largest infrared telescope ever launched into space and is the final mission in NASA's 4 Great Observatories Program with the Hubble Space Telescope (HST), Compton Gamma-Ray Observatory (CGRO), and the Chandra X-Ray Observatory (CXO).It has three instruments on-board: 1) IRAC (Infrared Array Camera) an infrared camera which operates simultaneously on four wavelengths (3.6 μm, 4.5 μm, 5.8 μm and 8 μm), 2) IRS (Infrared Spectrograph), an infrared spectrometer with four sub-modules which operate at the wavelength ranges 5.3-14 μm (low resolution), 10-19.5 μm (high resolution), 14-40 μm (low resolution), and 19-37μm (high resolution) and 3) MIPS (Multiband Imaging Photometer of Spitzer), an imaging camera that detects light in the far-infrared, at wavelengths of 24, 70 and 160 microns.

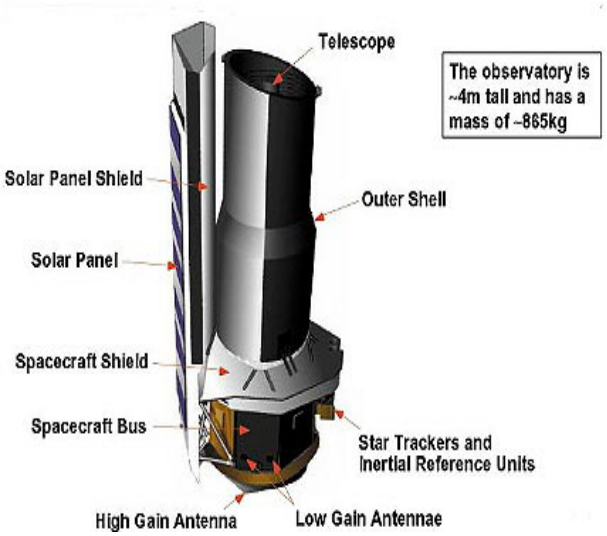

Figure 14: Spitzer Space Telescope.

The data we use for this analysis are taken from MIPS. The detector array for the 24 micron mode is 128×128 pixels, and is made of silicon that has been specially treated with arsenic. The 70 micron and 160 micron arrays are much smaller 32×32 and 20×20 pixels. Both are made of germanium treated with gallium. The 70 micron detector array is also used to take the very low resolution spectra from 50-100 microns.

The feed of view of the MIPS 24 detector is 5×5 arcminutes. At 160 microns it observes a smaller patch of sky measuring 0.5×5 arcminutes.

3.2 IR data reduction

We acquired data from the Spitzer space telescope that were obtained with the MIPS instrument in the 24 microns band. We obtained the post-BCD (post Basic Calibrated Data) data for the 9 galaxies in the sample that have available MIPS 24μm data. The data sets consist of several exposures that are interpolated into one mosaic image. From these images we measure the surface brightness in units of MJy/sr. The post-BCD product mosaic pixel sizes are 2.42×2.45 arcsec^2 for the 24 microns detector.

We perform aperture photometry using funtools. We define an aperture for the source with an ellipse that includes the total flux of the source and an elliptical annulus for the background region as depicted in Figures 15 - 16 for the 9 galaxies. In order to calculate the total flux density of each source, we sum the total flux of the source, subtract the background, on a set of pixels and multiply by the number of steradian per pixel. We convert the surface brightness to the flux density with the following formula:

$$f_v = \sum_{pixels} 2.45 \times 2.45 \frac{arc\,\mathrm{sec}^2}{pixel} \times 0.023504 \frac{Flux}{arc\,\mathrm{sec}^2}[mJy]. \qquad (11)$$

The flux density is converted to monochromatic flux:

$$F = \frac{c}{\lambda} f_v(\lambda). \qquad (12)$$

The uncertainty on the flux is calculated from the mosaic variance image by adding in quadrature the uncertainty of all pixels within the source aperture.

Finally, the monochromatic luminosity at 24μm is derived from the known formula:

$$L(24\mu m) = 4\pi D^2 F(24\mu m). \qquad (13)$$

We note that the X-ray sources for the galaxies SBS 0940+544 and I Zw18 do not seem to coincide with the 24μm emission of the galaxies.

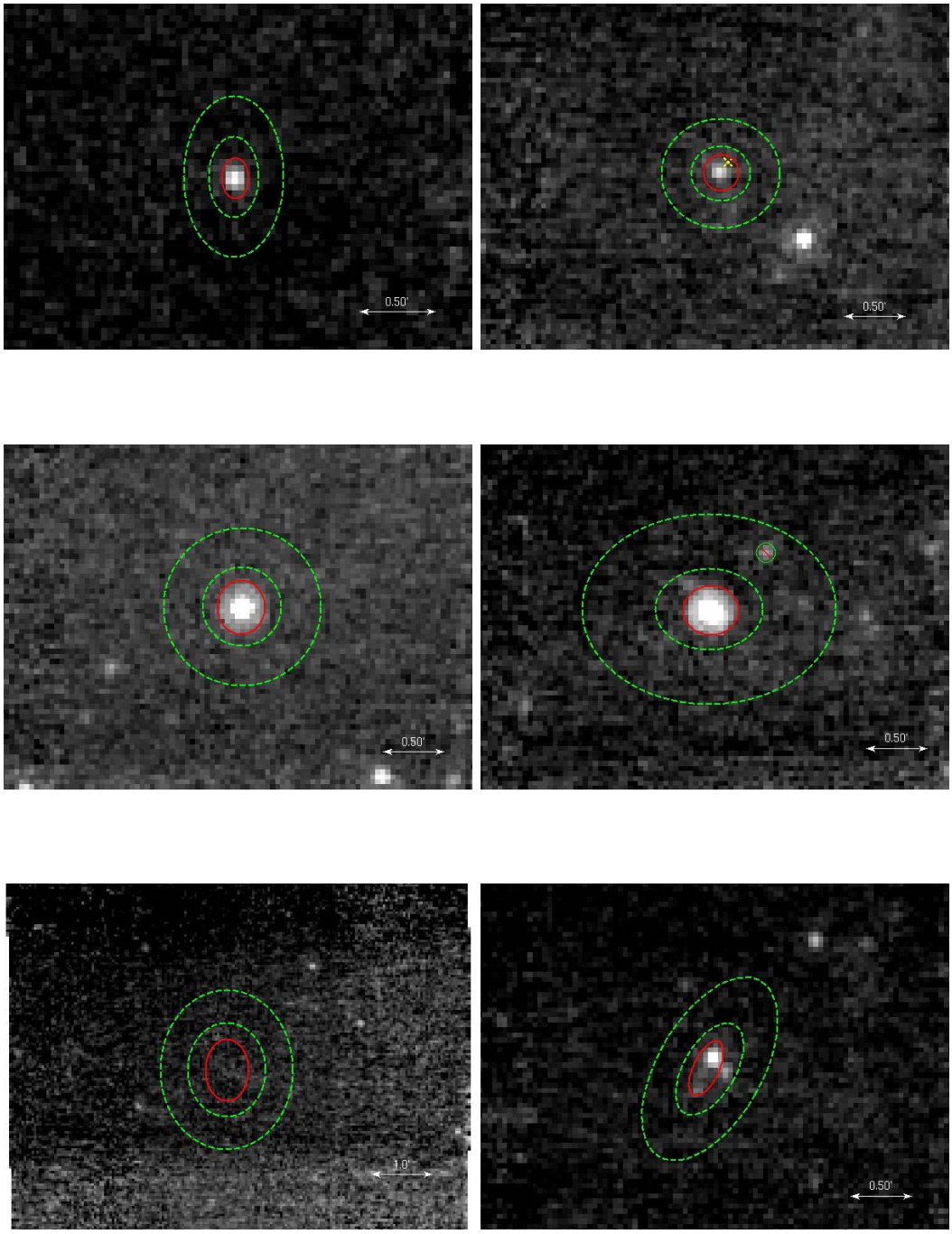

Figure 15: 24μm images of the galaxies: HS 0822+3542, SBS 0940+544, KUG 1013+381, SBS 1415+437, UGCA 292 and HS 1442+4250. The red region depicts the source, the green region the background and the pink X point where the X-ray source is located.

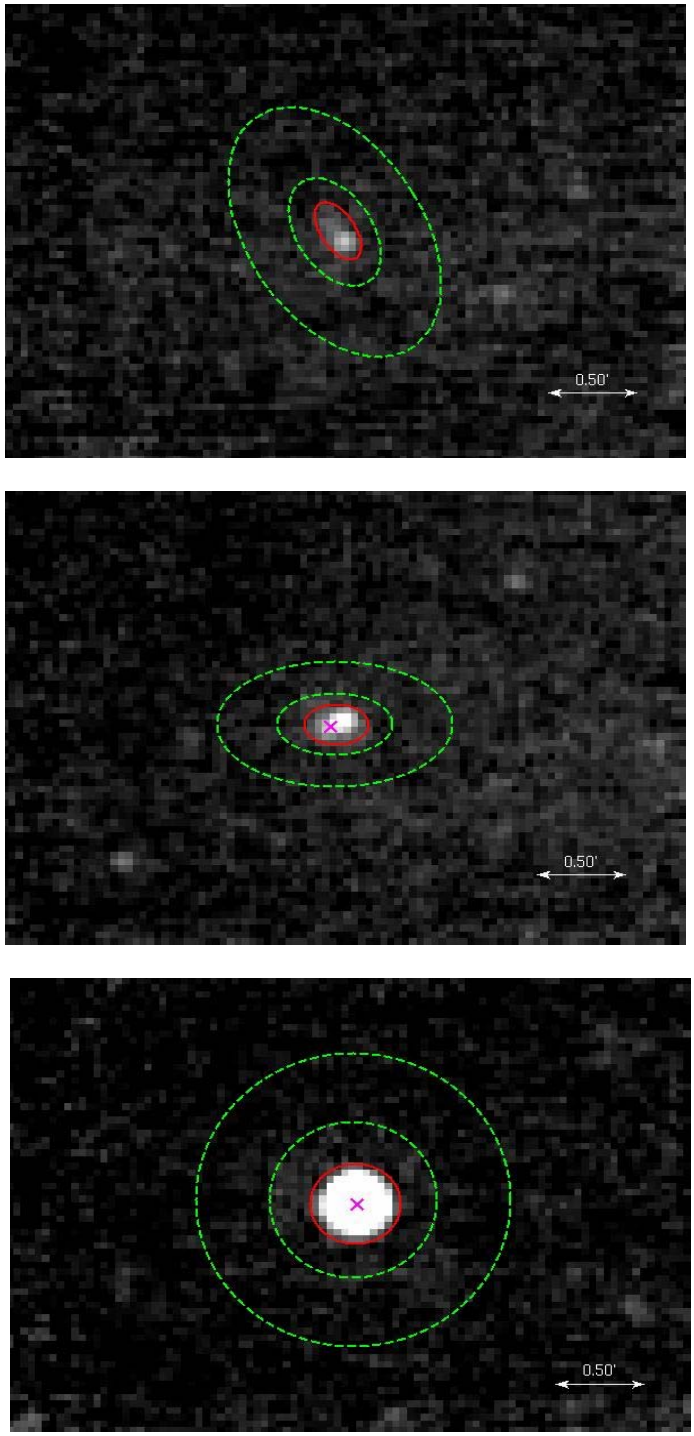

Figure 16: 24μm images of the galaxies: SBS 1102+606, I Zw18 and SBS 0335-052. The red region depicts the source, the green region the backgroundand the pink X point where the X-ray source is located.

3.3 Star Formation Rate

The star-formation rate (SFR) has been proven that correlates with the production of HMXBs (Grimm et al., 2003). SFR can be defined by the direct emission from young stars (UV continuum) and the gaseous emission lines (H_α, [OII]). Other SFR indicators are based on dust emission. The radiation from young stars is absorbed by dust and re-emitted in infrared. Infrared SFR indicators are complementary to UV/optical indicators because the latter are strongly affected by dust attenuation. Since, for practical reasons, it is difficult to extrapolate the bolometric IR emission, we use the monochromatic IR emission in measuring the SFR.

For this analysis, we will use the 24μm wavelength as a tracer of SFR which is considered a reliable indicator. Most of the 24μm emission comes from single photon transient heating of small grains. Calzetti et al. (2007) proposes the following SFR formula by calibrating H_{II} regions in nearby galaxies:

$$SFR(M_\odot yr^{-1}) = 1.31 \times 10^{-38}[L_{24\mu m}(ergs/sec)]^{0.885}, \quad (14)$$

for intermediate luminosity galaxies:

$$1{\times}10^{40} < \mathrm{L}_{24\mu m} < 3{\times}10^{44} \text{ erg/sec}$$

We calculate the SFR of our galaxy sample using the 24μm photometry described earlier. The results are listed at Table 10. We must take into consideration that measuring the SFR at the 24μm wavelength we underestimate the SFR since dwarfs lack of dust. We note that SBS 0335-052 appears to have very high SFR in comparison with the other XMPGs.

Table 10: 24 microns measurements and SFRs

Galaxy	Flux density (mJy)	Flux (10^{-13} erg/sec/cm^2)	L_{24} (10^{40} erg/sec)	SFR ($M_{\odot}yr^{-1}$)
UGC 772				
SDSS J210455.31-003522.2				
SBS 1129+576				
HS 0822+3542	2.23±0.09	2.78±0.12	0.54±0.02	0.002±0.001
SDSS J120122.32+021108.5				
RC2 A1116+51				
SBS 0940+544	1.60±0.10	2.01±0.13	1.47±0.09	0.005±0.003
KUG 1013+381	14.54±0.17	18.2±0.21	8.37±0.09	0.022±0.002
SBS 1415+437	16.67±0.15	20.8±0.19	2.70±0.02	0.008±0.001
6dF J0405204-364859				
SDSS J141454.13-020822.9				
SDSS J223036.79-000636.9				
UGCA 292	<0.87±0.31	1.09±0.34	0.08±0.03	0.0003±0.0010
HS 1442+4250	3.23±0.11	4.03±0.14	0.53±0.02	0.002±0.001
KUG 0201-103				
SDSS J081239.52+483645.3				
SDSS J085946.92+392305.6				
KUG 0743+513				
KUG 0937+298				
KUG 0942+551				
SBS 1102+606	1.33±0.10	1.67±0.11	0.79±0.06	0.003±0.002
RC2 A1228+12				
I Zw 18	4.84±0.11	6.05±0.14	2.12±0.05	0.006±0.001
SBS 0335-052	67.25±0.20	84.10±0.25	278.94±0.84	0.480±0.013
SBS 0335-052W	0.14±0.04	0.018±0.005	0.58±0.17	0.002±0.005

NOTES: The SFR errors were calculated with error propagation. For the galaxy UGCA 292 we calculate the upper limits.

4 Discussion

We want to find any correlation between the population of ULXs and their metallicity environment. In this sense, we compare our sample with samples of different metallicity. An ideal comparison sample is the Spitzer Infrared Nearby Galaxies Survey (SINGS) since it has been well investigated.

4.1 The SINGS sample.

The Spitzer Infrared Nearby Galaxies Survey (Kennicutt et al., 2003) is a comprehensive imaging and spectroscopic study of 75 nearby galaxies with distances < 30 Mpc. The morphological types of the sample range from elliptical to irregular. The SINGS sample does not include absolute extremes in properties that can be found in larger volumes such as ULIRGs, luminous AGNs or extremely metal poor galaxies.

Calzetti et al. (2007) selected a sub-sample of 33 galaxies from SINGS with available Hubble Space Telescope (HST) NICMOS images in the Paα hydrogen emission line (1.8756 μm) and Hα observations. The Hα and the Paα lines are used to measure the extinction correction. Furthermore, the Paα line is used to calibrate the mid-infrared emission.

The 33 galaxies are divided into three groups according to their oxygen abundance: High-metallicity galaxies [12+log(O/H) $\geq$ 8.35], Intermediate-metallicity galaxies [8.00 $<$ 12+log(O/H) $\leq$ 8.35], and Low-metallicity galaxies [12+log(O/H) $\leq$ 8.00]. For reference, the XMPGs have metallicities 12+log(O/H) $\leq$ 7.65 In Table 11 there is the list with the main characteristics of the SINGS sample.

4.2 The SINGS measurements.

For the SINGS galaxies we estimate the SFR using the calibration of Calzetti et al. (2010):

$$SFR = 5.5 \cdot 10^{-42} \times [L(H\alpha)_{obs} + 0.02L(24\mu m)] \quad (15)$$

Table 11: Characteristics of the SINGS sample.

Galaxy	Morphology	Distance (Mpc)	12+log(O/H)
High-metallicity galaxies			
NGC 0925	SAB(s)d	9.12	8.24-8.78
NGC 1512	SB(r)ab	10.5	8.37-9.05
NGC 2403	SAB(s)cd	3.5	8.31-8.81
NGC 2841	SA(r)b	9.8	8.52-9.19
NGC 2976	SAc	3.5	8.30-8.98
NGC 3184	SAB(rs)cd	11.10	8.48-9.14
NGC 3198	SB(rs)c	13.68	8.32-8.87
NGC 3351	SB(r)b	10.1	8.60-9.22
NGC 3627	SAB(s)b	8.7	8.49-9.10
NGC 3938	SA(s)c	12.2	8.35-9.07
NGC 4125	E6	21.4	8.58-9.21
NGC 4559	SAB(rs)cd	11.1	8.25-8.79
NGC 4569	SAB(rs)ab	16.58	8.56-9.19
NGC 4625	SAB(rs)m	9.17	8.27-9.04
NGC 4736	(R)SA(r)ab	5.3	8.31-9.01
NGC 4826	(R)SA(rs)ab	5.6	8.59-9.24
NGC 5033	SA(s)c	13.28	8.27-8.90
NGC 5055	SA(rs)bc	7.82	8.42-9.13
NGC 5194	SA(s)bc	8.2	8.54-9.18
NGC 5195	SB0_1	8.2	8.28-8.83
NGC 5866	S0_3	12.1	8.43-9.02
NGC 6946	SAB(rs)cd	5.0	8.40-9.04
NGC 7331	SA(s)b	15.1	8.40-9.05
Intermediate-Metallicity Galaxies			
NGC 1705	SA0-	5.1	8.20-8.43
IC 2574	SAB(s)m	2.8	7.94-8.26
NGC 4236	SB(s)dm	4.45	8.07-8.56
IC 4710	SB(s)m	7.8	8.11-8.62
NGC 6822	IB(s)m	0.47	8.04-8.67
Low-Metallicity Galaxies			
Ho II	Im	3.5	7.68-8.07
DDO 053	Im	3.56	7.77-8.13
Ho IX	Im	3.3	7.61-7.98
M81 dwB	Im	6.5	7.85-8.20
NGC 5408	IB(s)m	4.8	7.81-8.23
Discarded Galaxies			
NGC 0024	SA(s)c	8.8	8.32-8.92
NGC 1291	(R_1)SB(I))/a	10.5	8.42-9.01
M81 dwA	I?	3.55	7.34-7.64
NGC 3034	I0	5.2	8.36-9.09
NGC 4631	SB(s)d	8.5	8.13-8.76
DDO 154	IB(s)m	4.3	7.54-8.02

NOTES: Galaxy morphologies are from the NASA/IPAC Extragalactic Database (NED). Adopted distances as derived by Masters (2005). Oxygen abundances are from Moustakas et al. (2007). The 6 discarded galaxies by Calzetti et al. show problems with infrared data.

Note that the $L(H\alpha)_{obs}$ is the observed Hα luminosity without correction for internal dust attenuation.

We use the measurements of the Hα and 24μm fluxes of Dale et al. (2007) and Kennicutt et al. (2008 & 2009).

In Table 12 we list the following information: Column (1): Galaxy name, Column (2): Flux density at 24μm (Dale et al., 2007). Column (3): Luminosity at 24μm derived from Column (1), Column (4): Integrated Hα+[N_{II}] emission-line flux (Kennicutt et al., 2008; 2009). Column (5): The adopted integrated [N_{II}] $\lambda\lambda$6548, 6583/ Hα ratio (sum of both components), (Kennicutt et al., 2008 & 2009). Column (6): Hα observed luminosity derived from Columns (5) and (6). Column (7): SFR calculated with formula (15). For galaxies that Hα luminosities were not available, we used only the infrared-based SFR given by formula (14) and for those with no infrared data we used the Hα-based SFR: SFR=5.5×10^{-42}L(Hα) of Kennicutt et al., 2009.

4.3 Number of ULXs in the SINGS sample.

We want to compare the number of ULXs between the SINGS and the XMPG samples that are divided in different metallicity groups. The results of this comparison will tell us if there is a correlation between the metallicity and the number of ULXs. The catalogue of Swartz et al. in 2004 gives the number of ULXs for most of the SINGS using archival data from the Chandra telescope. Since this catalogue does not include galaxies without ULXs, we used additional data from the catalogue of Liu & Bregman (2005) for some galaxies (especially those of intermediate and low metallicity).

Various studies have shown that the ULXs are correlated with SFR (Gilfanov, Grimm & Sunyaev, 2004; Mapelli et al., 2010). Therefore, we substract the effect of the SFR by normalizing the number of ULXs to the SFR in order to see any correlation between the N_{ULX} and metallicity in the SINGS and the XMPG samples. The number of ULXs of the SINGS sample and XMPGs are given in Tables 13 and 14.

4.4 Comparison between the SINGS and XMPGs samples.

In Table 15 we calculate the mean values of the number of ULXs per unit SFR in the two samples, dividing the SINGS sample into 3 sub-groups according to metallicity values (High, Intermediate and Low metallicity). The Intermediate metallicity group is not included in Table 15 since all values are zero. We notice that the N_{ULX} per SFR is anticorrelated with metallicity.

Table 12: SINGS measurements

Galaxy	F(24μm) (Jy)	L(24μm) (10^{43} erg/sec)	log f(Hα) (log erg/sec/cm^2)	[N$_{II}$]/Hα	L(Hα)$_{obs}$ (10^{40} erg/sec)	SFR (M$_\odot$/yr)
(1)	(2)	(3)	(4)	(5)	(6)	(7)
High-Metallicity Galaxies						
NGC 0925	0.95	1.18	-11.08	0.380	6.01	1.634
NGC 1512	0.46	0.96	-11.43	0.300	4.77	1.319
NGC 2403	5.84	0.86	-10.25	0.290	5.12	1.225
NGC 2841	0.91	2.71	-11.64	0.612	3.39	3.170
NGC 2976	1.37	0.26	-11.19	0.130	0.87	0.334
NGC 3184	1.43	2.64	-11.12	0.523	7.36	3.310
NGC 3198	1.08	3.03	-11.40	0.304	6.85	3.710
NGC 3351	2.58	3.37	-11.24	0.620	3.71	3.907
NGC 3627	7.42	9.79	-10.80	0.540	10.90	11.362
NGC 3938	1.09	2.93	-11.25	0.420	8.53	3.696
NGC 4125	0.08	0.54	-	-	-	0.865
NGC 4559	1.12	1.78	-10.97	0.281	10.60	2.545
NGC 4569	1.44	5.88	-11.53	0.992	4.84	6.731
NGC 4625	0.13	0.16	-12.03	0.550	0.61	0.215
NGC 4736	5.65	2.29	-10.74	0.710	3.45	2.709
NGC 4826	2.72	2.28	-11.04	0.510	4.05	2.732
NGC 5033	1.97	6.47	-11.23	0.480	10.50	7.690
NGC 5055	5.73	5.23	-10.80	0.500	7.71	6.172
NGC 5194	12.67	13.40	-10.42	0.600	20.10	15.847
NGC 5866	0.21	0.49	-	-	-	0.794
NGC 6946	20.37	14.10	-10.34	0.540	16.50	16.437
NGC 7331	4.36	13.80	-11.07	0.610	13.40	15.893
Intermediate-Metallicity Galaxies						
NGC 1705	0.056	0.02	-11.50	0.090	0.90	0.074
IC 2574	0.28	0.07	-11.23	0.170	0.97	0.128
NGC 4236	0.55	0.10	-10.96	0.240	1.30	0.183
IC 4710	0.12	0.13	-11.67	0.160	1.60	0.231
NGC 6822	3.18	0.01	-10.54	0.070	0.07	0.015
Low-Metallicity Galaxies						
Ho II	0.2	0.03	-11.28	0.130	0.64	0.073
DDO 53	0.029	0.005	-12.26	0.020	0.08	0.011
Ho IX	0.037	0.007	-13.07	0.040	0.01	0.009
M81 dwB	0.009	0.004	-12.86	0.050	0.04	0.007
NGC 5408	0.43	0.15	-11.33	0.120	1.16	0.023
Discarded Galaxies						
NGC 0024	0.14	0.12	-11.87	0.170	0.74	0.164
NGC 1291	0.57	0.80	-11.29	0.54	3.76	1.091
M81 dwA	0.018	0.003	-15.30	0.010	7.29×10^{-5}	0.004
NGC 3034	-	-	-10.09	0.300	9.19	0.646
NGC 4631	8.15	7.09	-10.46	0.450	16.70	8.719
DDO 154	0.0080	0.002	-12.73	0.040	0.04	0.005

Table 13: Number of ULXs in the SINGS sample.

Galaxy (1)	N_{ULX} (2)	N_{ULX}/SFR ($M_{\odot}{}^{-1}$ yr) (3)
High-metallicity galaxies		
NGC 0925	-	-
NGC 1512	-	-
NGC 2403	$1.00^{+2.32}_{-1.00}$	0.82
NGC 2841	-	-
NGC 2976	-	-
NGC 3184	$2.00^{+2.65}_{-2.00}$	0.60
NGC 3198	-	-
NGC 3351	-	-
NGC 3627	-	-
NGC 3938	-	-
NGC 4125	$3.00^{+2.93}_{-2.93}$	3.47
NGC 4559	$3.00^{+2.93}_{-2.93}$	1.18
NGC 4569	-	-
NGC 4625	-	-
NGC 4736	$1.00^{+2.32}_{-1.00}$	0.38
NGC 4826	-	-
NGC 5033	-	-
NGC 5055	$3.00^{+2.93}_{-2.93}$	0.49
NGC 5194	$7.00^{+3.78}_{-3.78}$	0.44
NGC 5866	-	-
NGC 6946	$5.00^{+3.40}_{-3.40}$	0.30
NGC 7331	$3.00^{+2.93}_{-2.93}$	0.19
Intermediate-metallicity galaxies		
NGC 1705	$0.00^{+1.87}_{-0.00}$	0.00
IC 2574	$0.00^{+1.87}_{-0.00}$	0.00
NGC 4236	$0.00^{+1.87}_{-0.00}$	0.00
IC 4710	-	-
NGC 6822	-	-
Low-metallicity galaxies		
Ho II	$1.00^{+2.32}_{-1.00}$	13.70
DDO 53	-	-
Ho IX	$0.00^{+1.87}_{-0.00}$	0.00
M81 dwB	-	-
NGC 5408	$1.00^{+2.32}_{-1.00}$	43.86
Discarded galaxies		
NGC 0024	-	-
NGC 1291	$2.00^{+2.65}_{-2.00}$	1.83
M81 dwA	-	-
NGC 3034	$6.00^{+3.60}_{-3.60}$	9.29
NGC 4631	$2.00^{+2.65}_{-2.00}$	0.23
DDO 154	-	-

NOTES: Column (2) shows the N_{ULX} with Gehrels error observed by Swartz et al., 2004; Column (3) shows the normalized N_{ULX} to the SFR that is calculated in section 4.1.

Table 14: Number of ULXs in the XMPG sample.

Galaxy	N_{ULX}	N_{ULX}/SFR ($M_{\odot}{}^{-1}$ yr)
(1)	(2)	(3)
UGC 772	$0.00^{+1.87}_{-0.00}$	-
SDSS J210455.31-003522.2	$0.00^{+1.87}_{-0.00}$	-
SBS 1129+576	$1.00^{+2.32}_{-1.00}$	-
HS 0822+3542	$0.00^{+1.87}_{-0.00}$	0.00
SDSS J120122.32+021108.5	$0.00^{+1.87}_{-0.00}$	-
RC2 A1116+51	$1.00^{+2.32}_{-1.00}$	-
SBS 0940+544	$1.00^{+2.32}_{-1.00}$	216.43
KUG 1013+381	$0.00^{+1.87}_{-0.00}$	0.00
SBS 1415+437	$0.00^{+1.87}_{-0.00}$	0.00
6dF J0405204-364859	$0.00^{+1.87}_{-0.00}$	-
SDSS J141454.13-020822.9	$0.00^{+1.87}_{-0.00}$	-
SDSS J223036.79-000636.9	$0.00^{+1.87}_{-0.00}$	-
UGCA 292	$0.00^{+1.87}_{-0.00}$	0.00
HS 1442+4250	$0.00^{+1.87}_{-0.00}$	0.00
KUG 0201-103	$0.00^{+1.87}_{-0.00}$	-
SDSS J081239.52+483645.3	$0.00^{+1.87}_{-0.00}$	-
SDSS J085946.92+392305.6	$0.00^{+1.87}_{-0.00}$	-
KUG 0743+513	$0.00^{+1.87}_{-0.00}$	-
KUG 0937+298	$0.00^{+1.87}_{-0.00}$	-
KUG 0942+551	$0.00^{+1.87}_{-0.00}$	-
SBS 1102+606	$0.00^{+1.87}_{-0.00}$	0.00
RC2 A1228+12	$0.00^{+1.87}_{-0.00}$	-
I ZW 18	$1.00^{+2.32}_{-1.00}$	156.29
SBS 0335-052	$1.00^{+2.32}_{-1.00}$	2.08
SBS 0335-052W	$1.00^{+2.32}_{-1.00}$	494.96

NOTE: Column (2) derives from section 2.5 and Column (3) from section 3.3.

Table 15: Comparison of the SINGS and XMPGs sample.

	High-metallicity	Low-metallicity	XMPGs
$\langle N_{ULX} \rangle$	3.11±0.63	0.67±0.33	0.40±0.16
$\langle N_{ULX}/SFR \rangle$	0.87±0.34	19.19±12.95	86.98±51.71
$\sum N_{ULX}$	28.00±6.36	2.00±2.66	3.00±2.93[a]
$\sum N_{ULX}/\sum SFR$	0.43±0.08	19.05±13.50	60.77±35.09[a]

NOTE: [a] The SBS 0335-052 galaxy is excluded from the XMPGs.

We have a clearer view of this anticorrelation in Figure 17, where each sub-group is represented by one point with SFR equal to the sum of the SFRs of its consisting galaxies ($\sum_{N_{galaxies}}^{N_{galaxies}} SFR$) and the number of ULXs is the sum of the number of ULXs ($\sum_{N_{galaxies}} N_{ULX}$). In the case of SBS 0335-052, we find that this galaxy has extremely high SFRs for a Blue Compact Dwarf galaxy and thus is presented separately in Figure 17. Additionally, the N_{ULX}/SFR for the two samples is presented in a histogram in Figure 18.

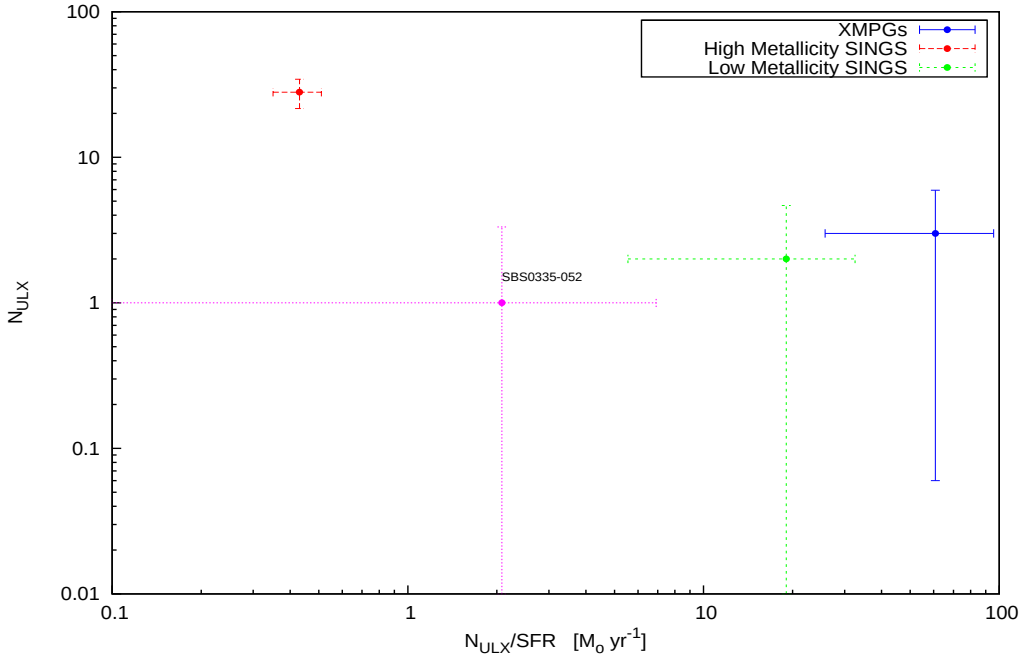

Figure 17: N_{ULX} versus N_{ULX}/SFR for the 3 group of galaxies.

We can see clearly in both Figures that the groups of galaxies are placed on the X-axis from high to low and to extremely low metallicity. As expected,

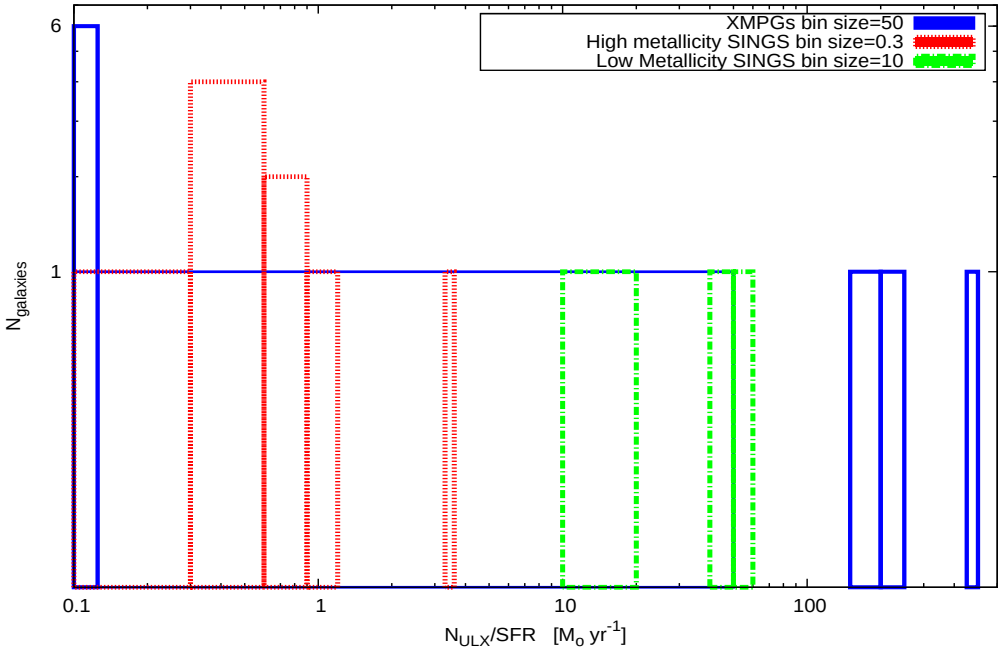

Figure 18: Histogram of the Number of galaxies versus N_{ULX}/SFR. The XMPGs that contain zero ULXs are in the first bin with size 0.1.

the N_{ULX} normalized to the SFR is inversely correlated to metallicity.

We check the statistical difference of the samples with two methods. The significance of the two means of our samples is: $t = \frac{\bar{x_1} - \bar{x_2}}{\sigma}$, where $\bar{x_1}$, $\bar{x_2}$ are the mean values of the 2 compared samples and σ is the standard deviation, $\sigma = \sqrt{{\delta x_1}^2 + {\delta x_2}^2}$. We take the mean values from Table 15. The difference between the XMPGs and High-metallicity SINGS is $\simeq 1.8\sigma$ and between the XMPGs and the Intermediate/Low-metallicity SINGS is $\simeq 1.5\sigma$. These results say that the mean values of these samples are not different enough with respect to their errors at a confident level.

We perform as well the Kolmogorov-Smirnov (K-S) test to see if the samples are drawn from two different distributions. This statistic quantifies the maximum vertical distance between the two cumulative distribution functions. We find that between the XMPGs and the High-metallicity SINGS, the propability for the two samples to be from the same distribution is 7%, while between the XMPGs and the Intermediate/Low-metallicity SINGS is even greater. These results do not help reject the hypothesis that the samples come from different populations.

These tests show that the anticorrelation between metallicity and the

number of ULXs is not a highly statistically significant level. However, we see that there is a trend showing that the number of ULXs increases from the high metallicity galaxies to the metal poor. This supports the scenario that ULXs prefer low metallicity environments as they can form easier massive stellar black holes and can reach high luminosities without exceeding the Eddington limit.

Moreover, our observational results come in agreement with models of HMXB formation in different metallicities (Linden et al., 2010). These models predict that the ULX population can derive from HMXBs found preferentially in low metallicity environments. These HMXBs probably evolved through common envelope and transfer mass through Roche-lobe overflow achieving high accretion rates. However, this model is not connected with the ULX formation of massive black holes from the collapse of massive stars in low metallicity environments since it is difficult to find such black holes in HMXBs. HMXBs with super-giant donors are not able to create ULXs because the mass transfer through stellar winds is weak and, moreover, it is difficult to create massive black holes through common envelope phase.

4.5 Conclusions

In this work, we investigated the ULX population in the most metal poor galaxies and reached the conclusion that we see a trend for XMPGs to host high number of ULXs when compared to their SFR, that derives from the comparison of different metallicity samples. The main problems we faced are that the number of galaxies is too small and the error bars are large to support confidently this anticorrelation. In addition, there was a lack of SFR measurements for most objects. However, we see indications that metallicity plays an important role in understanding the formation of ULXs.

The anticorrelation of metallicity with the number of ULXs can explain ULXs as part of the HMXB population without requiring exotic formation mechanisms at least for the majority of them.

In conclusion, larger galaxy samples should be studied for a better understanding of this field, as ULXs seem to form a wide, inhomogeneous group.

References

[1] Maraschi, L., Treves, A., & van den Heuvel, E. P. J. 1976, NAT, 259, 292

[2] Tauris, T. M., & van den Heuvel, E. 2003, arXiv:astro-ph/0303456

[3] Long, K. S., & van Speybroeck, L. P. 1983, Accretion-Driven Stellar X-ray Sources, 117

[4] Liu, J.-F., & Bregman, J. N. 2005, ApJS, 157, 59

[5] Swartz, D. A., Ghosh, K. K., Tennant, A. F., & Wu, K. 2004, ApJS, 154, 519

[6] Belczynski, K., Bulik, T., Fryer, C. L., Ruiter, A., Valsecchi, F., Vink, J. S., & Hurley, J. R. 2010, ApJ, 714, 1217

[7] Niemeyer, J. C., & Jedamzik, K. 1999, Phys. Rev. D, 59, 124013

[8] Madau, P., & Rees, M. J. 2001, ApJL, 551, L27

[9] Bahcall, J. N., & Ostriker, J. P. 1975, Nature, 256, 23

[10] Portegies Zwart, S. F., Baumgardt, H., Hut, P., Makino, J., & McMillan, S. L. W. 2004, Nature, 428, 724

[11] King, A. R., Davies, M. B., Ward, M. J., Fabbiano, G., & Elvis, M. 2001, ApJ, 552, L109

[12] Körding, E., Falcke, H., & Markoff, S. 2002, A&A, 382, L13

[13] Mirabel, I. F., & Rodríguez, L. F. 1999, ARA&A, 37, 409

[14] Miller, J. M., Fabian, A. C., & Miller, M. C. 2004, ApJ, 614, L117

[15] Matsushita, S., Kawabe, R., Matsumoto, H., Tsuru, T. G., Kohno, K., Morita, K.-I., Okumura, S. K., & Vila-Vilaró, B. 2000, ApJL, 545, L107

[16] Fabbiano, G., Zezas, A., & Murray, S. S. 2001, ApJ, 554, 1035

[17] Zezas, A., & Fabbiano, G. 2002, ApJ, 577, 726

[18] Kunth, D., & Ostlin, G. 2000, A&A Review, Volume 10, Issue 1/2, pp. 1-79

[19] Thuan, T. X., Izotov, Y. I., & Lipovetsky, V. A. 1997, ApJ, 477, 661

[20] Searle, L., & Sargent, W. L. W. 1972, ApJ, 173, 25

[21] Lee, H., Skillman, E. D.,Cannon, J. M., Jackson, D. C., Gehrz, R. D., Polomski, E. F., & Woodward, C. E. 2006, ApJ, 647, 970

[22] Swartz, D. A., Soria, R., & Tennant, A. F. 2008, ApJ, 684, 282

[23] Zampieri, L., Colpi, M., Mapelli, M., Patruno, A., & Roberts, T. P. 2010, American Institute of Physics Conference Series, 1248, 97

[24] Soria, R., Cropper, M., & Motch, C. 2005, Chinese Journal of Astronomy and Astrophysics Supplement, 5, 153

[25] Liu, J.-F., Bregman, J., Miller, J., & Kaaret, P. 2007, ApJ, 661, 165

[26] Vink, J. S., de Koter, A., & Lamers, H. J. G. L. M. 2001, A&A, 369, 574

[27] Thuan, T. X., Bauer, F. E., Papaderos, P., & Izotov, Y. I. 2004, ApJ, 606, 213

[28] Freeman, P. E., Kashyap, V., Rosner, R., & Lamb, D. Q. 2002, ApJS, 138, 185

[29] de Vaucouleurs, G. 1991, Science, 254, 1667

[30] Gehrels, N. 1986, ApJ, 303, 336

[31] Dickey, J. M., & Lockman, F. J. 1990, Annual review of astronomy and astrophysics, Vol.28, 215

[32] Zezas, A., Fabbiano, G., Baldi, A., Schweizer, F., King, A. R., Rots, A. H., & Ponman, T. J. 2007, ApJ, 661, 135

[33] Grimm, H.-J., Gilfanov, M., & Sunyaev, R. 2003, MNRAS, 339, 793

[34] Calzetti, D., et al. 2007, ApJ, 666, 870

[35] Kennicutt, R. C., et al. 2003, Bulletin of the American Astronomical Society, 35, 1351

[36] Dale, D. A., et al. 2007, ApJ, 655, 863

[37] Masters, K. L. 2005, Ph.D. Thesis, Cornell University

[38] Moustakas, J., & Kennicutt, R. C. J. 2007, VizieR Online Data Catalog, 216, 40081

[39] Kennicutt, R. C., Jr., Lee, J. C., Funes, S. J., José G., Sakai, S., & Akiyama, S. 2008, ApJS, 178, 247

[40] Kennicutt, R. C., et al. 2009, ApJ, 703, 1672

[41] Calzetti, D., et al. 2010, ApJ, 714, 1256

[42] Gilfanov, M., Grimm, H.-J., & Sunyaev, R. 2004, Nuclear Physics B Proceedings Supplements, 132, 369

[43] Mapelli, M., Ripamonti, E., Zampieri, L., Colpi, M., & Bressan, A. 2010, MNRAS, 408, 234

[44] Linden, T., Kalogera, V., Sepinsky, J. F., Prestwich, A., Zezas, A., & Gallagher, J. S. 2010, ApJ, 725, 1984

Acknowledgements

Firstly, I would like to thank my supervisor Andrea Zezas for his support and great patience and for offering me the opportunity for the amazing period at the CfA.

I would like also to thank the Ph.D. student Paolo Bonfini for the time he sacrificed helping me and of course all my fellow students that supported me during the year of my Master.